

TEMPORAL EVOLUTION OF PAIR ATTENUATION SIGNATURES IN GAMMA-RAY BURST SPECTRA

MATTHEW G. BARING

Department of Physics and Astronomy MS-108,
Rice University, P.O. Box 1892, Houston, TX 77251, U.S.A.
baring@rice.edu

To appear in The Astrophysical Journal, Vol 649, October 1, 2006 issue.

ABSTRACT

The spectra obtained above 100 MeV by the EGRET experiment aboard the Compton Gamma-Ray Observatory for a handful of gamma-ray bursts has given no indication of any spectral attenuation that might preclude detection of bursts at higher energies. With the discovery of optical afterglows and counterparts to bursts in the last few years, enabling the determination of significant redshifts for these sources, it is anticipated that profound spectral attenuation will arise in the Gamma-Ray Large Area Space Telescope (GLAST) energy band of 30 MeV–300 GeV for many if not most bursts. This paper explores time-dependent expectations for burst spectral properties in the EGRET/GLAST band, focusing on how attenuation of photons by pair creation internal to the source generates distinctive spectral signatures. The energy of spectral breaks and the associated spectral indices provide valuable information that constrains the bulk Lorentz factor of the GRB outflow at a given time. Moreover, the distinct temporal behavior that is present for internal attenuation is easily distinguished from extrinsic absorption due to intervening cosmic background fields. These characteristics define palpable observational goals for both spaced-based hard gamma-ray experiments such as GLAST, and ground-based Čerenkov telescopes, and strongly impact the observability of bursts above 300 MeV.

Subject headings: gamma-rays: bursts — radiation mechanisms: non-thermal — gamma rays: theory
— relativity

1. INTRODUCTION

High energy gamma-rays have been observed for six gamma-ray bursts by the EGRET experiment on the Compton Gamma-Ray Observatory (CGRO). Most conspicuous among these observations is the emission of an 18 GeV photon by the GRB940217 burst (Hurley, et al. 1994). An additional case of interest is provided by the so-called MILAGRITO burst (Atkins et al. 2000; Atkins et al. 2003), GRB 970417, with its uncorroborated detection of $\sim 3\sigma$ significance in the TeV band. Taking into account EGRET's field of view, its detections indicate that emission in the 1 MeV–10 GeV range is probably common among bursts, if not universal (see Dingus 1995 for a discussion of EGRET high energy burst statistics). One implication of GRB observability at energies around or above 1 MeV is that, at these energies, spectral attenuation by two-photon pair production ($\gamma\gamma \rightarrow e^+e^-$) is absent in the source. From this fact, Schmidt (1978) deduced that a typical burst had to be closer than a few kpc, if it produced quasi-isotropic radiation.

In the aftermath of BATSE's revelation (e.g. Meegan et al. 1996) that most if not all long bursts are at cosmological distances, Krolik & Pier (1991) and Fenimore et al. (1992) proposed that GRB photon angular distributions are highly beamed, being produced by a relativistically-moving plasma, a suggestion that has become an underpinning of the GRB paradigm. This can dramatically reduce $\tau_{\gamma\gamma}$ below the $\sim 10^{11} - 10^{12}$ values realized for isotropic photons, and blueshift spectral attenuation turnovers above the observed spectral range. Determinations of the bulk Lorentz factor Γ of the GRB medium have mostly concentrated (e.g. Epstein 1985; Krolik & Pier 1991; Baring 1993) on cases where the angular extent of the source was of the order of $1/\Gamma$. These calculations generally assume an infinite power-law burst spectrum, and deduce (e.g.

Woods & Loeb 1995; Baring & Harding 1997b) that gamma-ray transparency up to the maximum energy detected by EGRET requires $\Gamma \gtrsim 100 - 10^3$ for cosmological bursts. Since BeppoSax spawned the age of precise determination of GRB redshifts, such bounds can now be refined for the BeppoSax, HETE and Swift databases; the discovery of high redshift bursts (e.g. see Cummings et al. 2005; Kawai et al. 2005; Berger et al. 2006; Haislip et al. 2006, for Swift bursts) might suggest even higher estimates of bulk Lorentz factors in those sources.

While the power-law source spectrum assumption is expedient, the spectral curvature seen in virtually all GRBs by BATSE (Band et al. 1993; Preece et al. 2000) is expected to play an important role in reducing the opacity for super-GeV and TeV band emission from these sources (Baring & Harding 1997a). Such curvature is patently evident in 200 keV–2 MeV spectra of some EGRET-detected bursts (e.g. Schaefer, et al. 1992), and its prevalence is indicated by the generally steep EGRET spectra for bursts (e.g. Hurley, et al. 1994; Schneid, et al. 1992; Sommer et al. 1994). This curvature profoundly impacts $\gamma\gamma$ opacity determinations, yielding a huge dearth of target soft photons in comparison with power-law spectra extrapolated down to the classic X-ray band. Hence, when considering emergent photons of dimensionless energies $\varepsilon_\gamma \gtrsim \Gamma^2/\varepsilon_B$, where ε_B is the dimensionless energy (in units of $m_e c^2$) of the spectral break in the BATSE band, the target photon energy is below $\varepsilon_B m_e c^2$ so that accurate pair opacity calculations mandate detailed treatment of the spectral curvature observed in bursts.

This paper enunciates the principal properties of pair production opacity that couple to spectral shape in the BATSE/EGRET energy range, embellishing upon and focusing the work of Baring & Harding (1997a), so as to identify possible observational diagnostics for the Gamma-Ray Large Area Space

Telescope (GLAST; <http://glast.gsfc.nasa.gov/>) mission and ground-based experiments such as the MILAGRO, MAGIC, HESS and VERITAS atmospheric Čerenkov telescopes. Moreover, it helps define GRB science drivers for future initiatives in the hard gamma-ray band above 100 MeV. These spectral signatures at energies where significant opacity is realized are clearly distinguishable from absorption by background radiation fields, and in particular via their time-dependent evolution. The fact that turnovers produced by constant Lorentz factor evolution can be easily discriminated from those generated by decelerating expansions is compelling. It may also be possible to elicit details of the adiabaticity or otherwise of the post-fireball expansion. Accordingly, hard γ -ray telescopes can, in principal, provide powerful probes on such evolution of bulk motions in bright bursts, which can then be used to generate useful bounds on the explosion energy, a key piece of information elucidating the nature of the central engine for bursts. Before discussing these evolutionary effects and the potential for observational diagnostics in Sections 3 and 4, the paper presents refinements in the formalism for pair production opacities in Section 2.

2. GAMMA-GAMMA PAIR PRODUCTION OPACITIES

In this Section, a detailed formalism for $\gamma\gamma$ pair creation opacities from piecewise-continuous power-law distributions of photons is expounded upon, extending the presentation of Baring & Harding (1997a) by providing greater detail and also compact analytic reduction of the integrals for the optical depths.

2.1. General Formalism for Internal Target Photons

To assess the role of two-photon pair production in attenuating gamma-ray burst spectra in the EGRET/GLAST band, the interactions of photons created only within the emission region are considered here, neglecting the presence of any external radiation; the impact of such external radiation fields on burst spectra is discussed in Section 2.4 below. The calculations of this subsection mirror those of Baring (1994), whose work is used as a basis for elucidating the effects of GRB spectral structure on pair production opacities. For simplicity, the photon distribution is assumed to be azimuthally symmetric about some beaming axis (that is presumably aligned near to the line of sight to a distant observer), with the spectrum $n(\varepsilon)$ being identical for all photon angles θ_ε relative to the axis within some cone of emission. Here ε is the photon energy in units of $m_e c^2$, a convention adopted throughout this paper. The photon distribution function then takes the form $n_\gamma(\varepsilon, \mu_\varepsilon) = n(\varepsilon) f(\mu_\varepsilon)$, with $f(\mu_\varepsilon)$ normalized to unity, and where $\mu_\varepsilon = \cos\theta_\varepsilon$ is the cosine of the photon angle with respect to the axis of symmetry. Further, for anisotropic (beamed) photons we take the simple case that the angular distribution about the axis is uniform within a cone of half-angle $\theta_\varepsilon = \theta_m$:

$$f(\mu_\varepsilon) = \frac{1}{1 - \mu_m} \quad , \quad \mu_m \equiv \cos\theta_m \leq \mu_\varepsilon \leq 1 \quad . \quad (1)$$

This conical sector form is not exactly equivalent to the angular distribution of an isotropic photon distribution boosted by some bulk Lorentz factor $\Gamma \sim 1/\theta_m$ with respect to an observer at infinity, since it lacks the “wings” at $\mu_\varepsilon \lesssim \mu_m$. Yet it suffices to exhibit the general nature of photon beaming effects on pair production rates. Consequently, the results presented here, for example that inferred from Eq. (17), differ slightly from what would be derived from a beamed adaptation of the isotropic results of Gould and Schreder (1967, as expounded briefly below),

which was the approach of Krolik & Pier (1991) and Fenimore, Epstein & Ho (1992). Scientific conclusions pertaining to relativistic beaming in GRBs are not contingent upon such subtleties, largely because the computed optical depths are most sensitive to the beaming factor θ_m , i.e. $1/\Gamma$, among the relevant parameters. Moreover, adherence to one particular angular distribution is not mandated by observations nor by theoretical insights. For example, diffusive particle acceleration at the relativistic shocks that are suggested as being sites for energization in gamma-ray bursts does not generate isotropic distributions at the shock in any frame of reference (e.g. see Bednarz & Ostrowski 1998; Kirk et al. 2000).

For photons that interact with themselves to produce pairs, a slight modification of the form for the pair production optical depth $\tau_{\gamma\gamma}(\varepsilon)$ in Eq. (7) of Stepney and Guilbert (1983) was adopted by Baring (1994) as a starting point for analytic developments. This form, appropriate for photon distributions independent of azimuthal angles, is

$$\begin{aligned} \tau_{\gamma\gamma}(\varepsilon) &= \frac{4R}{\pi} \int_{-1}^1 d\mu_\varepsilon f(\mu_\varepsilon) \int_{-1}^1 d\mu_\omega f(\mu_\omega) \int_0^\infty d\omega \frac{n(\omega)}{\varepsilon\omega} \\ &\quad \times \int_{\chi_-}^{\chi_+} \frac{\chi^3 \sigma_{\gamma\gamma}(\chi) d\chi}{\sqrt{(\chi_+^2 - \chi^2)(\chi^2 - \chi_-^2)}} \quad . \end{aligned} \quad (2)$$

Here $\chi = [\varepsilon\omega(1 - \cos\Theta)/2]^{1/2}$ is the center-of-momentum (CM) frame energy of the photons, whose energies and angle cosines in the observer’s frame are $(\varepsilon, \mu_\varepsilon)$ and (ω, μ_ω) respectively. Θ is the angle between the photon directions. The pair production threshold condition is then $\chi \geq 1$. Since $\mu_\varepsilon = \cos\theta_\varepsilon$ and $\mu_\omega = \cos\theta_\omega$, the range $[0, \pi]$ of azimuthal angles in the observer’s frame establishes the bounds

$$\chi_\pm^2 = \frac{\varepsilon\omega}{2} \left\{ 1 - \cos(\theta_\varepsilon \pm \theta_\omega) \right\} \quad . \quad (3)$$

The focus of Baring (1994) was on infinite power-law *number density* distributions $n(\omega)$. In this paper, low energy cutoffs with $\omega > 0$ will be introduced, since these prove expedient in treating piecewise continuous broken power-laws, which constitute suitable approximations to the general shape of burst spectra. Specifically, the form

$$n(\varepsilon) = \begin{cases} 0 & , \quad \varepsilon < \varepsilon_C \\ n_\gamma \varepsilon^{-\alpha} & , \quad \varepsilon > \varepsilon_C \end{cases} \quad (4)$$

is used for some minimum photon energy $\varepsilon_C m_e c^2$, following Gould and Schreder (1967) and Baring & Harding (1997a); note that the works of Baring (1993, 1994) used an integral photon flux index. The units of both n_γ and $n(\varepsilon)$ correspond to inverse volumes. The change of variables $\zeta = (1 - \cos\Theta)/2 = \chi^2/\varepsilon\omega$ can then be employed to facilitate the manipulation of the integrals along the lines of Baring (1994). Defining a parameter

$$\eta = \sqrt{\varepsilon\varepsilon_C} \quad , \quad (5)$$

that is the center-of-momentum frame energy for head-on photon collisions, the form

$$\tau_{\gamma\gamma}(\varepsilon) = n_\gamma \sigma_T R \mathcal{T}_\alpha(\theta_m, \sqrt{\varepsilon\varepsilon_C}) \varepsilon^{\alpha-1} \quad , \quad (6)$$

is obtained, where

$$\mathcal{T}_\alpha(\theta_m, \eta) \equiv \frac{4}{\sigma_T} \int_1^\infty d\chi \frac{\sigma_{\gamma\gamma}(\chi)}{\chi^{2\alpha-1}} \mathcal{F}_\alpha(\theta_m, \eta, \chi) \quad (7)$$

is an integration over the pair production cross-section $\sigma_{\gamma\gamma}$, and the angular distributions contribute the factor

$$\mathcal{F}_\alpha(\theta_m, \eta, \chi) = \frac{1}{\pi} \int_{\mu_m}^1 \frac{d\mu_\varepsilon}{1-\mu_m} \int_{\mu_m}^1 \frac{d\mu_\omega}{1-\mu_m} \int_{\zeta_-}^{\zeta_+} \frac{\zeta^\alpha d\zeta}{\sqrt{(\zeta_+ - \zeta)(\zeta - \zeta_-)}} \Theta\left(\frac{\eta^2 \zeta}{\chi^2}\right). \quad (8)$$

Here, $\Theta(x)$ is a Heaviside step function such that $\Theta(x) = 1$ for $0 \leq x \leq 1$ and is zero otherwise. It expresses the kinematic condition $\chi^2 \geq \varepsilon \varepsilon_c \zeta$ for $\zeta = (1 - \cos\Theta)/2$ that is imposed by the spectral truncation. The ζ -integration limits are $\zeta_\pm = \chi_\pm^2 / \varepsilon \omega = [1 - \cos(\theta_\varepsilon \pm \theta_\omega)]/2$. Note that in the case of $\varepsilon_c = 0$, effecting the substitution $\alpha \rightarrow \alpha + 1$ in these results reproduces those of Baring (1994).

It is elucidating to focus first on the case of isotropic photons, i.e. when $\theta_m = \pi$. The angular integrations in Equation (8) are facilitated by following Baring (1994) and changing variables to ϕ with $2\zeta = \{\zeta_+ + \zeta_- + (\zeta_+ - \zeta_-) \cos\phi\}$, and then performing the solid angle transformation $(\mu_\omega, \phi) \rightarrow (\mu_{\varepsilon\omega}, \phi_{\varepsilon\omega})$, where $\mu_{\varepsilon\omega} = \cos\Theta$ is the cosine of the angle between the photons. This results in a dramatic simplification of the three integrals. Defining

$$q = \min\left\{1, \frac{\chi}{\eta}\right\}, \quad (9)$$

Equation (8) becomes, in the limit $\theta_m \rightarrow \pi$,

$$\mathcal{F}_\alpha(\pi, \eta, \chi) = \frac{q^{2(\alpha+1)}}{\alpha+1}, \quad (10)$$

with the $\eta \leq 1$ case (i.e. infinite power-law; $q = 1$) reproducing Eq. (10) of Baring (1994). It then follows that

$$\mathcal{T}_\alpha(\pi, \eta) = \frac{\mathcal{H}(\alpha, \eta)}{\alpha+1} \quad (11)$$

where

$$\mathcal{H}(\alpha, \eta) = \frac{4}{\sigma_\tau} \int_1^\infty \frac{q^{2(\alpha+1)}}{\chi^{2\alpha-1}} \sigma_{\gamma\gamma}(\chi) d\chi. \quad (12)$$

This completely defines the pair production optical depth for the case of an isotropic distribution of photons with a power-law spectrum that is truncated at low energies, a result that is quickly shown to be equivalent to Eqs. (21)–(23) of Gould and Schreder (1967) by observing their notation $s \rightarrow \chi^2$, and by performing the appropriate integration by parts.

An exact expression for $\mathcal{T}_\alpha(\pi, 1)$ was obtained by Svensson (1987; see his Equation [B6]), and can be approximated (Baring 1993, 1994) to better than 1% for $1 < \alpha < 7$ using $\mathcal{H}(\alpha, 1) \approx 7/6/\alpha^{5/3}$. An asymptotic form for $\eta \rightarrow \infty$ can be obtained most expediently by adopting a form equivalent to Equation (11):

$$\mathcal{T}_\alpha(\pi, \eta) \equiv \frac{8}{\sigma_\tau} \int_\eta^\infty \frac{d\chi}{\chi^{2\alpha+3}} \int_1^\chi x^3 \sigma_{\gamma\gamma}(x) dx. \quad (13)$$

Using the asymptotic form $\sigma_{\gamma\gamma}(x) \approx (3\sigma_\tau/8) [2 \log_e 2x - 1]/x^2$ for $x \gg 1$, i.e. for the extreme Klein-Nishina domain, one quickly arrives at

$$\mathcal{T}_\alpha(\pi, \eta) \approx \frac{3}{2\alpha} \frac{1}{\eta^{2\alpha}} \left\{ \log_e 2\eta - 1 + \frac{1}{2\alpha} \right\}, \quad \eta \gg 1. \quad (14)$$

This is identical to Eq. (24a) of Gould and Schreder (1967).

2.2. Angular Contributions for Strong Beaming

Exploration of the angular integrals for cases $\mu_m \neq -1$, and specifically those where beaming is strong and $\mu_m \approx 1$, is not as straightforward as the isotropic photon situation. Equation (8) must be manipulated considerably to extract compact analytic forms. In the limit $1 - \mu_m \approx \theta_m^2/2 \ll 1$, to leading order in $(1 - \mu_m)$, it is easily shown that $\zeta_\pm \approx (\sqrt{1 - \mu_\varepsilon} \pm \sqrt{1 - \mu_\omega})^2/2$, suggesting the change of integration variables to κ such that $\zeta = \kappa^2(1 - \mu_m)/2$ together with $1 - \mu_\varepsilon = (1 - \mu_m)x_\varepsilon^2$ and $1 - \mu_\omega = (1 - \mu_m)x_\omega^2$. This yields the following form for \mathcal{F}_α :

$$\mathcal{F}_\alpha(\theta_m, \eta, \chi) \approx \frac{16 \theta_m^{2\alpha}}{2^{2\alpha} \pi} \int_0^1 x_\varepsilon dx_\varepsilon \int_0^{x_\varepsilon} x_\omega dx_\omega \times \int_{\kappa_-}^{\kappa_+} \frac{\kappa^{2\alpha+1} d\kappa}{\sqrt{[(\kappa_+)^2 - \kappa^2][\kappa^2 - (\kappa_-)^2]}} \Theta\left(\frac{\kappa \eta \theta_m}{2\chi}\right), \quad \theta_m \ll 1, \quad (15)$$

for $\kappa_\pm = x_\varepsilon \pm x_\omega$. Here, the fact that the integration is symmetric under the interchange $x_\varepsilon \leftrightarrow x_\omega$ has been used to write $x_\omega \leq x_\varepsilon$ without loss of generality, thereby introducing an extra factor of two.

Before evaluating Eq. (15) in generality, it is instructive to identify compact results in two asymptotic regimes. In the particular case of infinite power-law spectra, where $\eta = 0$, the value of \mathcal{F}_α is independent of χ so that the angular integrations separate from the energy ones. Then, further changes of variables along the lines of $x_\omega = wx_\varepsilon$ and $\kappa^2 = x_\varepsilon^2[(1-w)^2 + 4wz]$ leads to evaluation of the integrals using identities 3.197.3, 9.134.3 and 7.512.4 from Gradshteyn & Ryzhik (1980):

$$\mathcal{F}_\alpha(\theta_m) \approx \mathcal{A}(\alpha) \theta_m^{2\alpha}, \quad (16)$$

$$\mathcal{A}(\alpha) = \frac{2^{1-2\alpha} \Gamma(2\alpha+2)}{\Gamma(\alpha+2) \Gamma(\alpha+3)},$$

valid for $\eta \theta_m / \chi \ll 1$. This result is precisely that in Eq. (12) of Baring (1994) after the adjustment for the different spectral index convention used there; Baring (1994) also posited an approximation, $\mathcal{A}(\alpha) \approx 2/(4/3 + \alpha)^{27/11}$ that is accurate to better than 1% on $1 < \alpha < 7$. Equation (16) implies

$$\mathcal{T}_\alpha(\theta_m, \eta) \approx \mathcal{A}(\alpha) \mathcal{H}(\alpha, 1) \theta_m^{2\alpha}, \quad \eta \theta_m \leq 1. \quad (17)$$

This can be inserted into Eq. (6) to obtain the corresponding final result for the pair production optical depth for cases where the beaming is strong, but when the spectral cutoff of the photon distribution does not come into play.

The opposite asymptotic limit arises for $\eta \theta_m / \chi \gg 1$, and is readily tractable since it samples $\kappa \ll 1$ and $x_\varepsilon \approx x_\omega$ domains. This results in

$$\mathcal{F}_\alpha(\theta_m, \eta, \chi) \approx \frac{4}{\alpha+1} \theta_m^{2\alpha} \left\{ \frac{\chi}{\eta \theta_m} \right\}^{2(\alpha+1)}, \quad \frac{\eta \theta_m}{\chi} \gg 1. \quad (18)$$

Comparison with Eq. (16) indicates that the coefficients for the $\eta \theta_m \ll \chi$ and $\eta \theta_m \gg \chi$ domains differ, largely due to the behavior of \mathcal{F}_α near the critical kinematic value of $\eta \theta_m = \chi$. Observe that this asymptotic domain establishes $\mathcal{F}_\alpha(\theta_m, \eta, \chi) \propto 1/\theta_m^2$, which is essentially a phase space factor in the angular integrals.

To reduce Eq. (15) for general values of $\eta\theta_m/\chi$, a moderate amount of manipulation is required. An effective approach is to change the integration variables via $x_\omega = wx_\varepsilon$ and $\kappa = x_\varepsilon\rho$, so that x_ε , w and ρ constitute the new set of variables. The w integration is then performed first, leading to the appearance of a simple inverse trigonometric function. The procedure is detailed in the Appendix, where it is found that \mathcal{F}_α is expressible in terms of elementary functions and the hypergeometric function $F \equiv {}_2F_1$. The attractively compact result of these manipulations is (for $\theta_m \ll 1$)

$$\mathcal{F}_\alpha(\theta_m, \eta, \chi) \approx \theta_m^{2\alpha} \begin{cases} \mathcal{A}(\alpha), & \Psi \geq 1; \\ \mathcal{G}_\alpha(\Psi), & 0 \leq \Psi \leq 1, \end{cases} \quad (19)$$

where $\Psi = \chi/(\eta\theta_m)$, and $\mathcal{G}_\alpha(\Psi)$ is given by Eq. (A4):

$$\mathcal{G}_\alpha(\Psi) = \frac{8}{\pi} \Psi^{2(1+\alpha)} \left\{ \frac{\arccos \Psi}{\alpha+1} - \frac{\Psi\sqrt{1-\Psi^2}}{\alpha+2} + \frac{\Psi F(1/2, \alpha+3/2; \alpha+5/2; \Psi^2)}{(\alpha+1)(2\alpha+3)(\alpha+2)} \right\}. \quad (20)$$

Accordingly, much of the character of \mathcal{F}_α is encapsulated in the one parameter Ψ . Numerical protocols for the evaluation of the hypergeometric function $F(1/2, \alpha+3/2; \alpha+5/2; \Psi^2)$ are outlined in the Appendix. Observe that $\mathcal{G}_\alpha(\Psi) \leq \mathcal{A}(\alpha)$ for $0 \leq \Psi \leq 1$. Using this formalism, Eq. (7) can now be written

$$\mathcal{T}_\alpha(\theta_m, \eta) \approx \theta_m^{2\alpha} \mathcal{K}(\alpha, \eta\theta_m), \quad (21)$$

where

$$\mathcal{K}(\alpha, \eta) = \frac{4}{\sigma_\tau} \int_1^{\hat{\eta}} d\chi \frac{\sigma_{\gamma\gamma}(\chi)}{\chi^{2\alpha-1}} \mathcal{G}_\alpha\left(\frac{\chi}{\hat{\eta}}\right) + \mathcal{A}(\alpha) \int_{\hat{\eta}}^\infty d\chi \frac{\sigma_{\gamma\gamma}(\chi)}{\chi^{2\alpha-1}}, \quad \hat{\eta} = \max\{1, \eta\}. \quad (22)$$

The general character of $\mathcal{K}(\alpha, \eta)$ is illustrated in Fig. 1, including its comparison with the similar function $\mathcal{H}(\alpha, \eta)$ that pertains to the isotropic photon case above.

Further attempts to reduce the integration over χ in the expression for \mathcal{T}_α lead to undesirable algebraic complexity, introducing somewhat obscure special functions that preclude further insight. Hence numerical evaluations of the integral over χ suffice. These can be checked using two identifiable asymptotic formulae. The first is the $\eta\theta_m \leq 1$ form that is encapsulated in Eq. (17), which uses $\mathcal{K}(\alpha, \eta) \rightarrow \mathcal{K}(\alpha, 1) \equiv \mathcal{A}(\alpha) \mathcal{H}(\alpha, 1)$ for $\eta \leq 1$. The second is for the extreme Klein-Nishina limiting case of $\eta\theta_m \gg 1$, which can be obtained by inserting Eq. (19) into Eq. (7), and then invoking the integral evaluations in Eq. (A9). The result is

$$\mathcal{T}_\alpha(\theta_m, \eta) \approx \frac{3}{2\alpha} \frac{1}{\eta^{2\alpha}} \left\{ \log_e \eta\theta_m - \frac{3}{4} + \frac{1}{2\alpha} \right\}, \quad \eta\theta_m \gg 1, \quad (23)$$

which provides an excellent approximation to $\mathcal{T}_\alpha(\theta_m, \eta)$ for $\eta\theta_m \gtrsim 4$. The similarity of this to the Klein-Nishina asymptotic form for isotropic photons in Eq. (14) is noticeable, highlighting how in this domain, the extreme kinematic collimation imposed by the $\chi^2 \geq \eta^2(1 - \cos\Theta)/2$ condition is more constraining than the beaming of the photon distribution within

an angle θ_m . This characteristic is evinced in Fig. 1 via the approximate constancy of the ratio $\mathcal{K}(\alpha, \eta)/\mathcal{H}(\alpha, \eta)$ for large η : comparison of Eq. (23) with Eq. (14) reveals that $\mathcal{K}(\alpha, \eta)/\mathcal{H}(\alpha, \eta) \rightarrow \mathcal{A}(\alpha)/(\alpha+1)$ as $\eta \rightarrow \infty$.

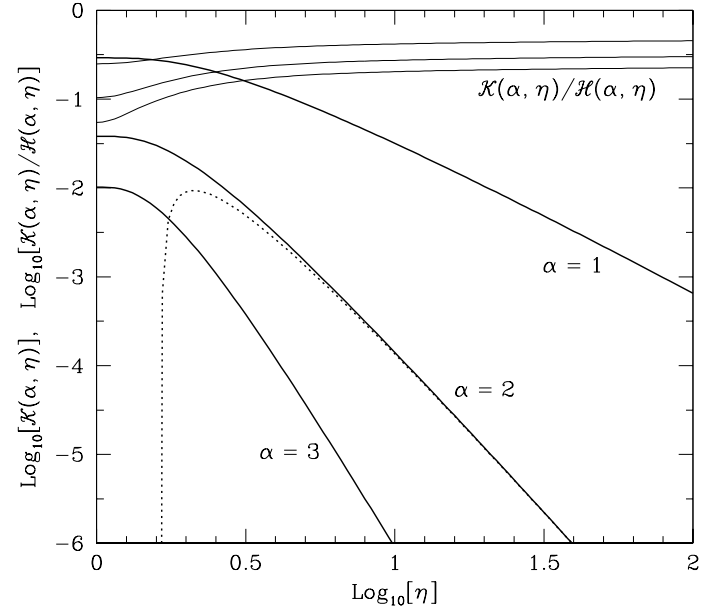


FIG. 1.— The general behavior of $\mathcal{K}(\alpha, \eta)$ is depicted as a function of η as the heavy-weight curves, for three values of the spectral index α , as indicated. Also exhibited as the dotted curve is the asymptotic approximation for $\mathcal{K}(\alpha, \eta)$ for $\eta \gg 1$, precisely Eq. (23) with the substitution $\theta_m \rightarrow 1$. To compare with the function $\mathcal{H}(\alpha, \eta)$ that appears in the formalism for isotropic photons, in the upper portion of the plot the values of the ratio $\mathcal{K}(\alpha, \eta)/\mathcal{H}(\alpha, \eta)$ are illustrated as lighter weight curves, specifically for the indices $\alpha = 1, 2, 3$ ranging from top to bottom.

For the practitioner desiring an even more compact approximation for the optical depth, a useful result that embodies the essence of both the two beamed forms in Eqs. (17) and (23) can be put forward. There is no unique choice, however a comparison of the coefficients in Eqs. (16) and (18) suggests the following mapping that mimics the appearance of the isotropic form:

$$\mathcal{F}_\alpha(\theta_m, \eta, \chi) \rightarrow \mathcal{A}(\alpha) Q^{2(\alpha+1)} \theta_m^{2\alpha}, \quad (24)$$

$$Q = \min\left\{1, \frac{\chi}{\mathcal{B}(\alpha)\eta\theta_m}\right\}.$$

Insertion of this into Eq. (7) then yields a development identical to that leading to Eqs. (11) and (12), but with the substitution $\eta \rightarrow \mathcal{B}(\alpha)\eta\theta_m$. Hence, in cases where $\mathcal{B}(\alpha)\eta\theta_m \leq 1$, this protocol automatically generates the result in Eq. (17). Comparison of Eq. (14), with $\eta \rightarrow \mathcal{B}(\alpha)\eta\theta_m$, and Eq. (23) then establishes the correspondence

$$\mathcal{B}(\alpha) = \left[(\alpha+1) \mathcal{A}(\alpha) \right]^{1/(2\alpha)} \quad (25)$$

from these Klein-Nishina limiting forms, and the resulting compact approximation

$$\mathcal{T}_\alpha(\theta_m, \eta) \approx \mathcal{A}(\alpha) \mathcal{H}\left(\alpha, \mathcal{B}(\alpha)\eta\theta_m\right) \theta_m^{2\alpha} \quad (26)$$

is generally accurate to around 10–20% for $\eta\theta_m \gtrsim 1$. Note that $\mathcal{B}(\alpha)$ is of the order of magnitude of unity for typical α .

This approximation essentially maps over to a correspondence of $\mathcal{B}(\alpha)\theta_m \leftrightarrow 1/\Gamma$ between beaming angle and bulk Lorentz factor Γ of the emission region. Clearly such an approximation is subjective, but does not compromise the appropriateness of pair production attenuation calculations. Notwithstanding, for the investigation here, Eqs. (21) and (22) will form the basis of the calculations below.

2.3. General Constructs for Complicated GRB Spectra

The adopted form for the approximate optical depth due to pair creation from a beamed conical power-law photon distribution with a low energy cutoff at dimensionless energy ε_C (generally $\ll 1$) is

$$\tau_{\gamma\gamma}(\varepsilon) = n_\gamma \sigma_T R \mathcal{K}\left(\alpha, \theta_m \sqrt{\varepsilon \varepsilon_C}\right) \theta_m^{2\alpha} \varepsilon^{\alpha-1} . \quad (27)$$

Here, given that the angular form in Eq. (1) is normalized to unity, the normalization parameter n_γ , defined in Eq. (4), is such that $n_\gamma \theta_m^{2\alpha}/(\alpha-1)$ represents the total photon number density above the pair production threshold $\varepsilon \sim 1/\theta_m$ for the beamed photon distribution. The expression corresponding to Eq. (27) for a power-law that extends down to zero energy but possesses a high-energy cutoff is obviously obtained by subtracting this result from that for an infinite power-law, namely Eq. (17). It is then a simple matter to construct optical depths for more complicated burst spectral structure. The particular spectrum that will be adopted throughout this paper is that used in Baring & Harding (1997a; hereafter BH97a), namely a power-law broken at a dimensionless energy ε_B with a low energy cut-off at ε_C :

$$n(\varepsilon) = n_\gamma \varepsilon_B^{-\alpha_h} \begin{cases} 0, & \text{if } \varepsilon \leq \varepsilon_C , \\ \varepsilon_B^{\alpha_l} \varepsilon^{-\alpha_l}, & \text{if } \varepsilon_C \leq \varepsilon \leq \varepsilon_B , \\ \varepsilon_B^{\alpha_h} \varepsilon^{-\alpha_h}, & \varepsilon > \varepsilon_B . \end{cases} \quad (28)$$

This form mimics the generic shape of burst spectra (see Table 1 below for a listing of pertinent spectral parameters for BATSE/EGRET bursts), and the introduction of a sharp cutoff at ε_C is to encompass scenarios where there is severe soft photon paucity. Note that typical burst radiation mechanisms such as synchrotron emission and inverse Compton scattering from quasi-isotropic particles formally generate spectra with $\varepsilon_C \rightarrow 0$, though in practice, the inverse Compton mechanism, so-called pitch angle synchrotron emission (e.g. see Epstein 1973), and moreover self-absorbed situations (e.g. Crider & Liang 1999; Granot, Piran & Sari 2000), produce extremely flat spectra so that finite choices of ε_C can be realistic. Using the formalism described above, the optical depth for pair production attenuation of such a broken power-law/truncated photon distribution is found to be

$$\frac{\tau_{\gamma\gamma}(\varepsilon)}{n_\gamma \sigma_T R} \approx \theta_m^{2\alpha_l} \left\{ \mathcal{K}(\alpha_l, \eta_C) - \mathcal{K}(\alpha_l, \eta_B) \right\} \frac{\varepsilon^{\alpha_l-1}}{\varepsilon_B^{\alpha_h-\alpha_l}} + \theta_m^{2\alpha_h} \mathcal{K}(\alpha_h, \eta_B) \varepsilon^{\alpha_h-1} , \quad (29)$$

where

$$\eta_B = \theta_m \sqrt{\varepsilon_B \varepsilon} , \quad \eta_C = \theta_m \sqrt{\varepsilon_C \varepsilon} . \quad (30)$$

Observe that at $\varepsilon \sim 1/(\varepsilon_B \theta_m^2)$ the two spectral terms in Eq. (29) become comparable, indicating that this energy is the domain where the attenuation ‘‘image’’ of the the BATSE-band spectral break at ε_B is experienced. This expression for the optical

depth, to be used hereafter in the computations of this paper, closely resembles that in Eq. (2) of BH97a, differing only by its use of \mathcal{K} functions in the place of \mathcal{H} functions and the replacement $\Gamma \rightarrow 1/\theta_m$; ensuing results in this paper are quantitatively but not qualitatively different from those in BH97a.

Clearly, more gradual spectral curvature can be treated by fitting the GRB continuum with piecewise continuous power-laws, generalizing the structure inherent in Eq. (29) to sums of various power-law factors combined with differences in \mathcal{K} functions. The technique presented here is well suited to this adaptation, though for typical burst spectral forms, only modest changes in $\tau_{\gamma\gamma}$ will be afforded by such refinement of the optical depth calculation, and then only deep into the attenuation trough. There may exist, of course, occasional pathological exceptions that require such refinement.

2.4. Cosmological Background Targets

The cosmic background infra-red (IR) and optical starlight fields provide target photons external to gamma-ray bursts that can attenuate in the EGRET/GLAST band. They effect line-of-sight absorption, and so are exponential functions of the line-of-sight optical depth. Moreover, they are independent of burst characteristics such as flux, variability and spectral evolution, and therefore are markers only of the distance or redshift to a given burst. Such a property is touted as a means of probing the background fields using any bursts (and active galaxies) detected by the atmospheric Čerenkov technique. The attenuation effect of intervening cosmic background fields on hard gamma-rays via $\gamma\gamma \rightarrow e^+e^-$ has been extensively studied in the context of active galaxies (e.g. Stecker, de Jager & Salamon 1992, MacMinn & Primack 1996; for reviews, see Primack et al. 2001, Stecker 2001), with predictions being sensitive to the assumed level of the infra-red background, a historically poorly measured quantity. This uncertainty has been pervasive in the discussion of absorption of TeV photons from active galaxies, predominantly for AGNs that are detected at TeV energies by atmospheric Čerenkov telescopes have been nearby (e.g. Mrk 421 and Mrk 501 are at $z = 0.031$ and $z = 0.034$, respectively). However, this discussion has experienced a profound development in the recent observation (Aharonian et al. 2006) by the HESS telescope array of harder than expected TeV-band spectra in two more distant blazars, H 2356-309 at $z = 0.165$ and 1ES 1101-232 at $z = 0.186$ (see also Albert et al. 2006b, for the very recent MAGIC detection of 1ES 1218+30.4 at $z = 0.182$). This extension to more distant sources has reduced the upper bounds on the extragalactic background IR light to interesting levels that are within 50% of lower limits set by galaxy counts with Hubble Space Telescope data. This advance moves the field of TeV gamma-ray astronomy much closer to being a powerful probe of these radiation backgrounds.

Line-of-sight attenuation of GRB spectra provides a very different case, at least for those bursts at moderate to high redshifts that were seen by the BeppoSax mission, and are currently being detected by Swift. Typical spectral attenuation expected in these sources was summarized by Mannheim, Hartmann & Funk (1996), and impacts the sub-100 GeV band when $z \gtrsim 1$. Stecker & de Jager (1996) concluded that the 18 GeV photon seen by EGRET from GRB 940217 imposed a constraint of $z \lesssim 2$ for this source in order to evade interaction with intervening background photons. In the burst context, the higher redshift pushes the target photons into the near IR and optical starlight bands, which are better measured at low to moderate

redshift than the classical IR field. Additional uncertainty is entailed in the evolution of such backgrounds with redshift during the epoch of rapid star formation, yet galaxy count data can yield fairly well constrained models for the evolving background (Kneiske, Mannheim & Hartmann 2002). Since the focus here is on internal pair creation in bursts that is germane to the EGRET/GLAST band, calculations of attenuation by cosmological backgrounds are beyond the scope of this presentation.

3. ATTENUATION OF GRB SPECTRA: EVOLUTIONARY EFFECTS

The GRB spectral forms adopted here have explicitly assumed, for simplicity, that there is only one radiation component contributing to the gamma-ray band. This is supported by the majority of EGRET burst data (see Table 1 for spectral indices), with the delayed 18 GeV photon in GRB 940217 providing only a suggestion of a second component. Evidence for additional components is contingent upon broad spectral coverage. Accordingly an interesting possibility has been offered by the so-called MILAGRITO burst (Atkins et al. 2000; Atkins et al. 2003), GRB 970417, a BATSE burst that was seen with $\sim 3\sigma$ significance in the TeV band by the water tank Čerenkov detector MILAGRITO that served as the prototype for MILAGRO. The extrapolation of the BATSE spectral data up to the TeV band falls over four decades below the claimed MILAGRITO flux (see Fig. 9 of Atkins et al. 2003), thereby arguing strongly for the existence of a second component. No other bursts have been seen by the MILAGRITO/MILAGRO experiment, nor other TeV-band telescopes, with MILAGRO (Atkins et al. 2005) and MAGIC (Albert et al. 2006a) providing interesting upper bounds to two bursts.

Multi-component theoretical models exist in the literature (e.g. Meszaros & Rees 1994; Meszaros, Rees & Papatanasious 1994; Katz 1994; Dermer, Chiang & Mitman 2000), so the relationship between the current analysis and models with several radiation components cannot be summarily dismissed. Inspection of the developments of Section 2 quickly reveals that the pair production optical depth formalism presented here is entirely valid for multiple component spectra as long as they use the BATSE band component as the population of target photons. The super-GeV spectra may differ tremendously due to the presence of additional components, however the attenuation factors will depend only on the known BATSE/EGRET spectral forms. Accordingly, the signatures presented here will be widely applicable to burst spectra in the EGRET/GLAST band, unless additional components emerge below 100 MeV.

In this paper, the analysis is restricted to cases of a single break in the single component power-law photon spectrum. This modest limitation is motivated by expediency, and can be relinquished when more accurate representations of a GRB source spectrum are desired. Such improvements can be effected by approximating the spectrum by a piecewise continuous broken power-law with a sufficient number of components to achieve the desired accuracy. Yet such refinements rarely prove necessary if the specialized form adopted here in Eq. (29) is tailored to agree with published Band model fits (Band et al. 1993; Preece et al. 2000). The reason for this centers on where the image of the target MeV photons is realized in the absorbed portion of the spectrum. The difference between the sharply broken power-law in Eq. (28) and the Band spectrum is manifested only near the break in the MeV band, leading to generally modest underpredictions of the attenuation factors, and then only near the depths of the troughs (that appear in Figures 2–4 below) in the band above 10 GeV. This is the low-flux portion of the

burst spectrum that will generally fall below current instrumental sensitivities, and in some cases be obscured by attenuation of cosmological background radiation fields. Accordingly the sharp breaks assumed here shall suffice for the present investigation.

3.1. Typical Absorption Characteristics

To complete the determination of optical depths, one requires knowledge of the source emission region size R and the number density (or spectral normalization parameter) n_γ of photons therein. For nearby bursts that sample Euclidean space, the coefficient n_γ can be obtained from the flux f_{511} at 511 keV per 511 keV energy interval via the simple relation $f_{511} = 4\pi n_\gamma cR^2/d^2$, where d is the distance to the source. For such an absence of cosmological corrections, the perceived source size R can be written as $R = R_v\Gamma^\lambda$, where Γ is the bulk Lorentz factor of the emission region with respect to the observer at infinity, and $R_v = c\Delta t$ is the effective size of the region as deduced from observed variability timescales Δt . Following Baring & Harding (1996, 1997b), the value of $R_v = 3 \times 10^7$ cm is adopted here, commensurate with BATSE and COMPTEL variability timescales of $\Delta t =$ ms, and anticipated variability timescales from the GLAST Gamma-Ray Burst Monitor (GBM). The index λ is chosen according to the presumed geometry and structure of the emission region. If the constraining structure scale (e.g. of clumpiness, or between colliding expanding shells) that defines source variability is along the line of sight (longitudinal) to the observer, then $\lambda = 2$. This is the preferred scenario in many GRB models that invoke colliding shells emanating perhaps from a central compact powerhouse. When the variability couples to structure transverse to the line of sight, then $\lambda = 1$, a situation that often appears in models of jet emission in active galactic nuclei. Such transverse variability was adopted by Baring & Harding (1997a,b). Theoretical arguments can be made for both $\lambda = 1$ and $\lambda = 2$ scenarios (or hybrids thereof), though observational discrimination between them is not yet afforded by the data. Both cases are considered in this paper, exhibiting only small qualitative differences between the two.

The earlier analyses of Baring (1993, 1994) and Baring & Harding (1996, 1997a,b) mentioned cosmological corrections only in passing, and moreover in an incomplete fashion, primarily because these works predated BeppoSax burst detections that spawned redshift determinations via their afterglows. At this juncture, there is an observational mandate to include correct redshift dependence in the pair production analysis. Such correction factors to the Euclidean (low z) case enter in several ways. The simplest one connects to the source variability, whose intrinsic timescale is actually $\Delta t/(1+z)$. This is the only redshift contribution to the inferred source size if the Lorentz factor Γ is assumed independent of redshift. This restriction on Γ may be inaccurate, since there can be a significant (and as yet unknown) correlation between the nature of the burst progenitor and circumburst environment and its redshift.

The major redshift dependence in the problem enters through the evolution of the source spectrum in its transmission to Earth. This receives contributions from the expansion of comoving volumes, which alters the perceived density of photons in the source, the redshifting of photon energy, and the frequency with which photons arrive at a detector. Spectral transmission calculations essentially connect to a luminosity transmission formalism, which is textbook and can be found, for example, in Chapter 5 of Longair (1998). The core property is that the comoving, isotropic bolometric source luminosity L_{bol} and the

detected bolometric *energy* flux S_{bol} are coupled via the *luminosity distance* d_L :

$$S_{\text{bol}} = \frac{L_{\text{bol}}}{4\pi d_L^2} = \frac{R^2}{d_L^2} S_{\text{GRB},z} . \quad (31)$$

Here $S_{\text{GRB},z} = L_{\text{bol}}/(4\pi R^2)$ is the GRB source flux at its outer periphery, i.e. at redshift z , and is a measure intrinsic to the source. While L_{bol} is integrated over solid angles, S_{bol} is independent of any collimation, provided the observer lies within the cone of collimation.

The luminosity distance thus encapsulates the evolution of the energy fluxes in the curved spacetime of the evolving universe, essentially coupling to the conservation of energy in the comoving frame. Observe that both S_{bol} and $S_{\text{GRB},z}$ possess units of energy per unit area per unit time (e.g. $\text{erg cm}^{-2} \text{sec}^{-1}$). For a particular choice of cosmology, the form for d_L is

$$d_L = \frac{c(1+z)}{H_0 \sqrt{|1-\Omega|}} S_k(\Theta) , \quad (32)$$

where H_0 is Hubble's constant, and for $k = \text{sgn}(\Omega_m + \Omega_\Lambda - 1)$,

$$S_k(\Theta) = \begin{cases} \sin \Theta, & k = 1, \\ \Theta, & k = 0, \\ \sinh \Theta, & k = -1, \end{cases} \quad (33)$$

is the factor in the Robertson-Walker metric that describes the solid angle modification from flat space. Its argument Θ is the *development angle*, and is given by

$$\Theta = \sqrt{|1-\Omega|} \int_0^z \frac{dz'}{E(z')} , \quad |1-\Omega| > 0 , \quad (34)$$

with $\Omega = \Omega_m + \Omega_\Lambda$ being the total density expressed as a fraction of the closure density $\rho_c = 3H_0^2/(8\pi G)$, and

$$E(z) = \sqrt{\Omega_m(1+z)^3 + \Omega_\Lambda + (1-\Omega)(1+z)^2} . \quad (35)$$

Here, the radiation contribution to the universe's dynamics is assumed negligible, as it is for the epochs since burst genesis. This form for the luminosity distance is employed in standard expositions on supernova probes of cosmology (e.g. Perlmutter, et al. 1997; Riess, et al. 1998).

In keeping with the results of those programs, and following on from the precise determinations of cosmology by WMAP microwave anisotropy observations (e.g. Spergel et al. 2003), here it is assumed that $H_0 = 0.72 \text{ km/sec Mpc}^{-1}$, and a choice of $\Omega_m = 0.27$ and $\Omega_\Lambda = 0.73$ is made (i.e. $\Omega \rightarrow 1$), corresponding to a flat space, $k = 0$ approximation. This simplifies the form of $E(z)$, and moreover the expression for d_L . Numerical integration of Eq. (34) is routine, and pertinent asymptotic limits are $\Theta \approx z \sqrt{|1-\Omega|}$ for $z \ll 1$, and $\Theta \rightarrow 2\sqrt{|1-\Omega|}/(1-\Omega_\Lambda)^{1/3} F(1/6, 2/3; 7/6; \Omega_\Lambda)$ for $z \rightarrow \infty$. These behaviors guide one to derive the useful analytic approximation for $\Omega_\Lambda = 1 - \Omega_m = 0.73$:

$$d_L \approx \frac{c}{H_0} \frac{z(1+z)}{1+0.29z} \left\{ 1 - \frac{z^2}{9(16+z^2)} \right\} , \quad (36)$$

which is accurate to better than around 2% for $0 < z < 40$, and generally better than 1% in the interval $1.7 < z < 40$.

Eq. (31) can be easily converted into a spectral equivalent, and moreover one appropriate for photon number densities, by

expressing the fluxes as integrals over differential photon spectra. For general spectral forms $n(\varepsilon)$, the GRB source flux can be written as

$$\begin{aligned} S_{\text{GRB},z} &= 4\pi m_e c^3 \int_0^\infty \varepsilon_z n(\varepsilon_z) d\varepsilon_z \\ &= 4\pi (1+z)^2 m_e c^3 \int_0^\infty \varepsilon_0 n([1+z]\varepsilon_0) d\varepsilon_0 , \end{aligned} \quad (37)$$

where $\varepsilon_z = [1+z]\varepsilon_0$ is the photon energy at the source corresponding to an observed dimensionless energy of ε_0 . An identical form to Eq. (37) is realized for S_{bol} , with the substitution $z \rightarrow 0$, so that the relationship between the integrands of the two flux forms reproduces Eq. (7) of Woods & Loeb (1995). For the purposes of normalization in this paper, if an observer detects a differential photon number flux spectrum $f(\varepsilon_0) = f_{511} \varepsilon_0^{-\alpha}$ above ε_c (with f_{511} in units of $\text{cm}^{-2} \text{sec}^{-1}$, and $f_{511}/(\alpha-1)$ being the total number flux above 511 keV), assuming $\varepsilon_c \ll 1$ for simplicity, then

$$S_{\text{bol}} = f_{511} m_e c^2 \int_{\varepsilon_c}^\infty \varepsilon_0^{1-\alpha} d\varepsilon_0 , \quad (38)$$

a result that is convergent for $\alpha > 2$. Then Eqs. (31), (37) and (38) can be combined to yield

$$f_{511} \equiv (0.511)^{1-\alpha} f(1 \text{ MeV}) = 4\pi n_\gamma c \frac{R^2}{d_L^2} (1+z)^{2-\alpha} , \quad (39)$$

independent of the choice of ε_c . Inversion of this result then leads to the specification of n_γ in terms of observables. Accordingly, the redshift dependence of the optical depth $\tau_{\gamma\gamma}$ is encapsulated entirely in the factor $d_L^2(1+z)^{\alpha-2}$, a result that can be inferred from Eq. (8) of Woods & Loeb (1995), and also Eq. (5.68) of Longair (1998). Note that this form contrasts the erroneous claim made by Lithwick & Sari (2001) that $\tau_{\gamma\gamma} \propto (1+z)^{2\alpha-2}$. In fact, just a single power α of $1+z$ should appear since, due to pair creation threshold kinematics, the optical depth must trace one power of the inverse of the target (i.e., observed) photon distribution, together with additional $1+z$ factors that are not directly connected to the spectrum.

Note that since $d_L \approx cz/H_0 \equiv d$ for $z \ll 1$, Eq. (39) reduces to the nearby source form $f_{511} = 4\pi n_\gamma c R^2/d^2$ in the $z \ll 1$ limit. In the implementations here, $\alpha \rightarrow \alpha_h$ is set. The relationship between the theoretical flux parameter f_{511} and the observed flux $f(1 \text{ MeV})$ at 1 MeV per MeV interval (tabulated for selected EGRET bursts in Table 1) is included in Eq. (39) for future reference. This concludes the formalism on cosmological input for the pair production attenuation problem.

The attenuation of a theoretical gamma-ray burst continuum can now be computed. Neglecting the influence of pair cascading, if the emission region is comparatively confined, the attenuation of a spectrum like that in Eq. (28) is exponential in the optical depth $\tau_{\gamma\gamma}$ given in Eq. (29). However, generally it can be distributed spatially with skin-depth effects in radiative transfer operating, so that the attenuation is by a factor of approximately $1/(1+\tau_{\gamma\gamma})$. Both cases are exhibited in the numerical results that follow. The principal spectral structure associated with pair production attenuation is illustrated in Fig. 2 for the BATSE/EGRET burst GRB930131, the so-called Super-bowl burst. This bright source exhibited the flattest spectrum of all EGRET bursts, and so is the prototype candidate for a burst easily detectable by GLAST at 100 MeV and above (see Band,

et al. 2004, Cohen-Tanugi, et al. 2004, or Omodei et al. 2006, for brief discussions of expected GLAST performance for burst detections). Since GRB 930131 pre-dated the determination of redshifts in optical afterglows, a redshift of $z = 1$ was assumed in the modeling (i.e., luminosity distance $d_L = 6.54$ Gpc), typical of BeppoSax and Swift long-duration bursts. Relevant source data are listed in Table 1, which is a composite and extension of Table 1 of Baring & Harding (1997a) and Table 2 of Baring & Harding (1997b). While such flux-selected bursts might well be at redshifts lower than unity, GRB 990123 at redshift $z \geq 1.61$ (Hjorth et al. 1999) provides a counterexample.

TABLE 1
SPECTRAL PARAMETERS FOR BATSE/EGRET BURSTS

GRB	BATSE ^a			EGRET/COMPTEL ^c		
	E_b (MeV)	α_l	α_h	$f(1 \text{ MeV})$ ($\text{cm}^{-2}\text{sec}^{-1}\text{MeV}^{-1}$)	α_h	ε_{MAX} (MeV)
910503	0.4 ± 0.2	0.7 ± 0.1	2.1	8.71 ± 0.49	2.2 ± 0.2	170
910601	0.6 ± 0.2	1.0 ± 0.1	2.4 ^b	0.50 ± 0.10^d	2.8 ± 0.2^d	5.0 ^d
910814	1.2 ± 0.1	0.9 ± 0.1	2.3 ^b	13.5 ± 0.85	2.8 ± 0.2	60
930131	0.7 ± 0.1	1.2 ± 0.1	2.5	1.95 ± 0.26	2.0 ± 0.2	1000
940217	0.8 ± 0.1	1.2 ± 0.2	2.4 ^b	0.36 ± 0.03	2.5 ± 0.2	3380 ^e
950425	0.4 ± 0.2^b	0.9 ± 0.1^b	1.8 ^b	1.62 ± 0.09	1.93 ± 0.04	120
990123	0.8 ± 0.2	0.6 ± 0.1	3.1	1.7 ± 0.2	2.8 ± 0.2^f	18

NOTE.— The time-averaged values of the break energy E_b , the spectral index below (α_l) and above (α_h) the break, the (measured or extrapolated) source photon flux at 1 MeV per MeV bin ($f(1 \text{ MeV})$), and the maximum energy ε_{MAX} of detection, for seven bursts observed with high significance by both BATSE and EGRET. All bursts listed were detected with the EGRET spark chamber, except for GRB 990123, which was seen in the TASC only (Briggs et al. 1999). (a) For the first three bursts, most BATSE parameters are taken from Band et al. (1993, the Band model fit), while BATSE data were obtained for GRB 930131 from Kouveliotou et al. (1994), for GRB 940217 from Hurley et al. (1994), for GRB 950425 from Catelli et al. (1996), and for GRB 990123 from Briggs et al. (1999). (b) These entries were obtained separately from an integration of the time-binned data archived in the electronic version of the BATSE Spectroscopy Catalog in Preece et al. (2000). (c) The high-energy spectral indices (α_h), fluxes and maximum energies as determined by EGRET and/or COMPTEL are from Schneid et al. (1992: GRB 910503) and Kwok et al. (1993: GRBs 910601 and 910814), Sommer et al. (1994: GRB 930131), Hurley et al. (1994: GRB 940217), Catelli et al. (1996: GRB 950425) and Briggs et al. (1999: GRB 990123). (d) These are COMPTEL measurements for GRB 910601 (see Hanlon, et al. 1994), quoted because COMPTEL detected it at a higher energy than did EGRET. (e) The notable 18 GeV photon from GRB 940217 was omitted here because it was not contemporaneous with any emission below 100 MeV. (f) This index from the OSSE/COMPTEL data was moderately consistent with the EGRET TASC value of 2.71 ± 0.1 that was subject to poorer statistics (see Briggs et al. 1999).

Spectra are presented for different Lorentz factors $\Gamma = 1/\theta_m$ (this coupling was adopted by Baring & Harding 1997a, though in general other $\Gamma \sim 1/\theta_m$ choices are equally acceptable), incorporating only internal absorption and not treating propagational attenuation through background radiation fields. The spectra indicate marked absorption whose onset energy couples mostly to the photon flux, source distance and Γ , as detailed, for example, in the extensive investigations of Baring (1993) and Baring & Harding (1997b), and also depends weakly on the EGRET band spectral index α_h . For $1/(1 + \tau_{\gamma\gamma})$ attenuation, above this turnover, the immediate spectral index is $2\alpha_h - 1$, which flattens to $\alpha_h + \alpha_l - 1$ at energies higher than Γ^2/ε_B , where the continuum below ε_B is sampled as the pool of target photons. Such inferences can be made by inspection of the two terms contributing to Eq. (29). These results resemble the character of the spectra illustrated in Baring & Harding (1997a) and Baring (2001), though note that higher Lorentz factors are appropriate here because of the greater luminosity distances involved (e.g. $d_L = 6.54$ Gpc here as opposed to 1 Gpc in Baring

2001). Spectra above around 30 GeV must, of course, be convolved with external absorption due to the cosmic infra-red and optical backgrounds for typical burst redshifts.

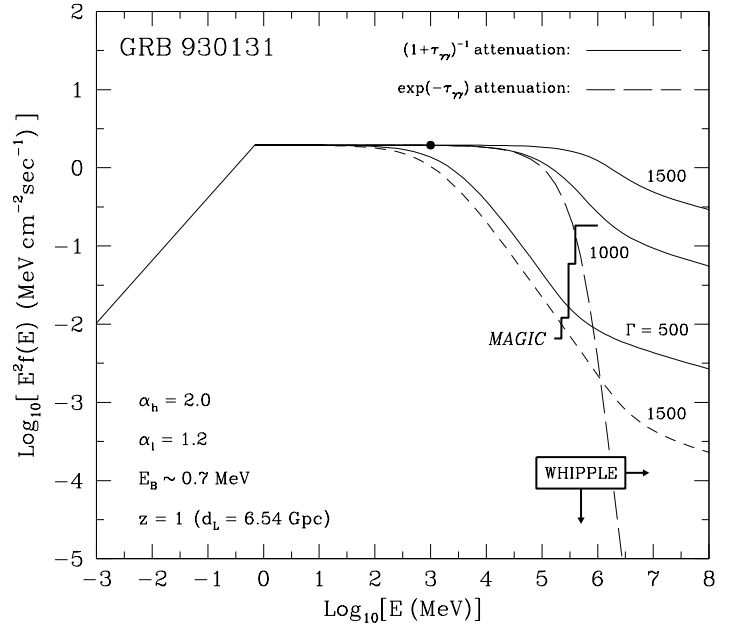


FIG. 2.— The $\gamma\gamma$ attenuation, internal to the source, for GRB 930131 for bulk Lorentz factors $\Gamma = 500, 1000, 1500$ of the emitting region, assuming a redshift $z = 1$ typical of long duration bursts. The source spectrum (in $\varepsilon^2 f(\varepsilon)$ format) was a power-law broken at $E_B = 0.7$ MeV, with spectral indices $\alpha_l = 1.2$ and $\alpha_h = 2.0$ (see Table 1). Cases of $1/(1 + \tau_{\gamma\gamma})$ attenuation (solid curves) and exponential attenuation (long dashed curve; $\Gamma = 1000$ only) are exhibited, for which a variability size of $R = 3 \times 10^7 \Gamma^2$ cm was assumed. Also, the short dashed line depicts a $\Gamma = 1500$, $1/(1 + \tau_{\gamma\gamma})$ attenuation example for $R = 3 \times 10^7 \Gamma$ cm. The filled circle denotes the highest energy EGRET photon at ~ 1000 MeV (Sommer et al. 1994). The threshold and sensitivity for the post- T_{90} Whipple observations of later bursts (Connaughton et al. 1997) is indicated by the “WHIPPLE” box, while the MAGIC upper bounds for GRB 050713a (Albert et al. 2006a) that coincided in part with the prompt emission are denoted by the heavyweight histogram.

The potential for observational diagnostics is immediately apparent. First, the extant EGRET data already provides a lower bound to Γ : the dot on Fig. 2 represents the highest energy photon from GRB930131, and clearly suggests that $\Gamma \gtrsim 700$ if the burst was at a redshift of $z \gtrsim 1$. It is also clear from the figure that the exponential and $1/(1 + \tau_{\gamma\gamma})$ attenuation signatures are strikingly different, so that a sensitive hard gamma-ray detector will easily be able to discriminate between these two possibilities. While realization of the $1/(1 + \tau_{\gamma\gamma})$ case is anticipated, should exponential attenuation be observed, it would be a profound diagnostic indicating that the emission region is relatively small, confined to a scale length shorter than the mean free path for pair attenuation. Comparison of the $R = 3 \times 10^7 \Gamma^2$ cm and $R = 3 \times 10^7 \Gamma$ cm examples for $\Gamma = 1500$ in Fig. 2 indicates that, in the absence of time-varying spectra, it will be difficult to discriminate between these longitudinal and transverse variability cases, since they cannot be clearly resolved from Lorentz factor inferences. Specifically, $R \propto \Gamma$ scenarios require slightly higher Γ for transparency at a given photon energy than do longitudinal variability cases.

To aid in the interpretation of pair attenuation it is useful to analytically determine the mean interacting (target) photon energy $\varepsilon_{\text{int}}(\varepsilon)$ for a given observed photon energy ε . This is computed as the ratio of an interaction probability like that

in Eq. (2), but with the extra weighting factor ω in the integrand, to the interaction probability with unit weighting factor. Retracing the analytic development in Sec. 2.1, it is quickly deduced, using the spectral form in Eq. (4) for the target photon population, that

$$\varepsilon_{\text{int}}(\varepsilon) \sim \frac{4}{\varepsilon\theta_m^2} \frac{\mathcal{K}(\alpha - 1, \eta_c\theta_m)}{\mathcal{K}(\alpha, \eta_c\theta_m)}. \quad (40)$$

For this spectral specialization, ε_c plays the approximate role of the break energy ε_B , though an alternative and slightly more involved form can easily be obtained to pertain to the spectrum in Eq. (28). Ratios of \mathcal{K} functions can be inferred from Fig. 1, and are typically of the order of a few for $\eta \sim 1$. Accordingly, for the specific example in Fig. 2, Eq. (40) clearly establishes that the attenuation image of the BATSE-band spectral break at ε_B appears at the energy $\varepsilon \sim 4\Gamma^2/\varepsilon_B$, which corresponds to the pair threshold condition in the bulk fluid rest frame, i.e., $(\varepsilon/\Gamma)(\varepsilon_B/\Gamma) \gtrsim 4$. This is generally at or above the threshold energy of atmospheric Čerenkov telescopes.

The first intensive TeV-band exploration of bursts was the Whipple Telescope campaign (Connaughton et al. 1997), whose results are typified by the “WHIPPLE” box in Fig. 2. This campaign in 1994-1995 consisted of targeted observations of nine BATSE bursts within, at best, around two minutes of trigger, coordinated via the BACODINE network. For each burst, the Whipple observations comprised 6 scans of around 30 minutes each with slightly offset sky positions (by $\approx 3^\circ$) to cover the BATSE error boxes. No TeV-band detections were made, and so the WHIPPLE box in Fig. 2 represents upper limits to the potential flux from the bursts studied in Connaughton et al. (1997). Due to the slewing times of a few minutes, these bounds are more germane to the burst afterglow phase, for which the MeV-band flux level is unknown. In contrast, the recent rapid-slewing observation (Albert et al. 2006a) of GRB 050713a by the MAGIC Telescope, triggered by a Swift alert, enabled a viewing of the burst at about 40 seconds after its onset, for a period of 37 minutes (Swift determined $T_{90} = 70 \pm 10$ sec). No gamma-ray signal was detected by MAGIC, and the resulting upper bounds are indicated in Fig. 2 as the heavyweight histogram. Since no redshift was determined for GRB 050713a, this sensitivity histogram corresponds to the $z = 1$ flux upper limit listed in Table 1 of Albert et al. (2006a). This flux limit is approximately commensurate with the fluence limits obtained by the MILAGRO Čerenkov water tank experiment for GRB 010921 (Atkins et al. 2005), the only burst surveyed in the MILAGRO campaign of 2000-2001 that possessed a moderately low, measured redshift ($z = 0.45$). STACEE also obtained a flux upper limit to GRB 050607 (Jarvis et al. 2005). The MAGIC sensitivity depicted in Fig. 2 is representative of the present capability of state-of-the-art atmospheric Čerenkov systems in terms of prompt GRB observations.

3.2. Time Evolution of Spectra

The photon counting statistics associated with EGRET burst detections generally only permitted using time-integrated spectra for the purposes of pair attenuation considerations. The enhanced sensitivity offered by GLAST by late 2007 may permit some exploration of time-dependent attenuation characteristics that are previewed in this Section, particularly if they emerge in bright bursts in the energy band below around 1 GeV.

There are a plethora of time-dependent gamma-ray burst spectral models in the literature, often pertaining to afterglow

evolution. For the prompt phase, there is evidence of prevalent hard-to-soft evolution on average in the BATSE database, though the spectral hardness development during a burst can often be more complicated (e.g. Ford et al. 1995, Preece et al. 1995). If the Lorentz factor Γ is effectively constant, then this observed variation could be due to evolving dissipational characteristics in the internal shocks, which are subtle and difficult to encapsulate in a cohesive manner. As an alternative scenario, the spectral evolution could primarily reflect the change in Γ on a timescale of the burst duration. For long-duration bursts with $T_{90} \sim 1 - 100$ sec, the physical scale associated with their duration is $\Gamma^2 c T_{90} \sim 3 \times 10^{15} - 3 \times 10^{18}$ cm for $\Gamma \sim 300 - 1000$. Hence bulk deceleration during the burst prompt phase is likely, and is a natural driver for GRB dissipation (e.g., Rees and Mészáros 1992). Both evolutionary possibilities are examined here.

The focus is first on a constant Γ , constant α_h scenario with the flux allowed to vary, for which representative spectra are displayed in Fig. 3 for the case of GRB 950425. There, the emission spectrum evolves only by an across-the-board decline of flux with time, displayed in increments of half a decade per “snapshot” (solid curves). Accordingly, this case does not explore adiabatic deceleration issues, or the role of radiative cooling, but does provide a definite correlation between evolution of the BATSE-band flux and the turnover energy E_t in the GLAST window. To elucidate this interesting diagnostic, observe that since the Lorentz factor is held constant, and at the turnover energy the last term in Eq. (29) provides the dominant contribution to $\tau_{\gamma\gamma}$, one finds that $\tau_{\gamma\gamma} \propto f(1 \text{ MeV}) E_t^{\alpha_h - 1}$. From this, it follows that the turnover energy couples to the MeV-band flux according to

$$E_t \propto [f(1 \text{ MeV})]^{-1/(\alpha_h - 1)}, \quad (41)$$

established using a $\tau_{\gamma\gamma} \sim 1$ criterion. For the GRB 950425 example in the Figure, this gives $E_t \sim [f(1 \text{ MeV})]^{-1/2}$. Combining this result with the $f(1 \text{ MeV}) E_t^{2 - \alpha_h}$ spectral form far above the break energy E_B then quickly yields

$$E_t^2 f(E_t) \propto E_t^{3 - 2\alpha_h} \propto [f(1 \text{ MeV})]^{(2\alpha_h - 3)/(\alpha_h - 1)} \quad (42)$$

as the mathematical form for the locus of turnover points in νF_ν space. For GRB 950425 this generates $E_t^{3 - 2\alpha_h} = E_t^{-0.92}$, since $\alpha_h = 1.93$, which is represented by the dashed curve in Fig. 3. Clearly, this correlation is extremely pronounced, and is a very useful probe of the constancy of Γ if the high energy spectral index does not evolve. In bright, flat-spectrum sources such as GRB 950425, GLAST may well be suited to investigating whether such character is exhibited, provided that the turnovers appear at below 1 GeV so that the LAT can accumulate enough photons in a typical burst duration. In particular, for the Γ adopted in this example, clearly the relative probability of seeing a super-100 MeV photon to observing a 1 MeV photon is enhanced at later times; whether this is connected to the detection (see Hurley et al. 1994) of the 18 GeV photon in GRB 940217 over an hour after burst trigger is undetermined. Note also that the attenuation results apply to any time-ordering of the curves, not just monotonically declining fluxes. Accordingly, one would infer a decline of the turnover energy in time in a rising flux precursor to the prompt GRB emission.

Another property of the attenuation is that well above the turnover energy, the results are approximately independent of $f(1 \text{ MeV})$, when ε_B is held fixed in time. This arises in the “recovery domain,” where the target photons are below ε_B and

the optical depth $\tau_{\gamma\gamma}$ is declining with energy till eventually the internal attenuation becomes insignificant (illustrated in Baring & Harding 1997b). At such energies higher than Γ^2/ε_B , as $\alpha_l = 0.9$ for GRB 950425, the optical depth is almost independent of the photon energy so that it mostly scales as $f(1 \text{ MeV})$. This behavior almost exactly cancels the normalization of the emission continuum so that the emergent spectrum is virtually independent of the MeV-band flux. For this source, given the location of the ACT sensitivity indicator in Fig. 3 (i.e. MAGIC flux upper limits for GRB 050713a), and the probable role of additional line-of-sight attenuation due to cosmic background radiation fields, the recovery domain is unlikely to be accessible to current generation Čerenkov telescopes.

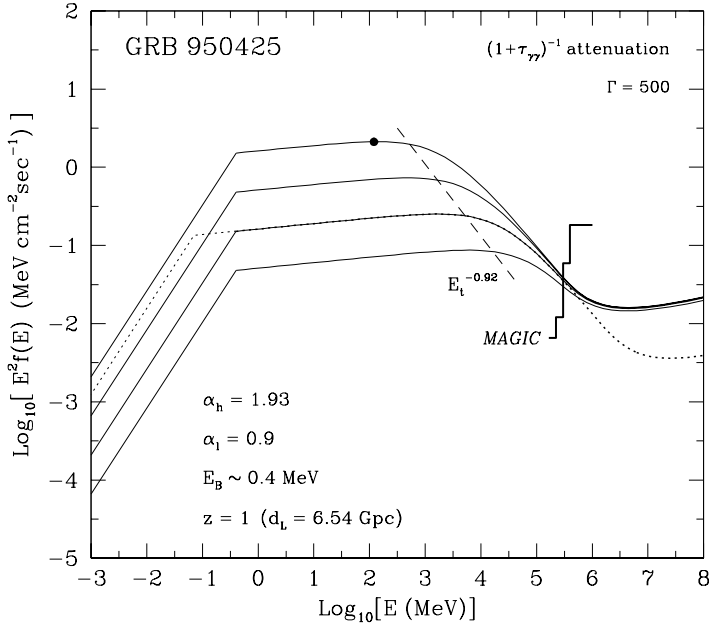


FIG. 3.— The $\gamma\text{-}\gamma$ attenuation, internal to the source, for GRB 950425 for bulk Lorentz factor $\Gamma = 500$, assuming a redshift $z = 1$ typical of long duration bursts. The source spectrum (in $\varepsilon^2 f(\varepsilon)$ format) was a power-law broken at $E_B = 0.4 \text{ MeV}$ (solid curves), with spectral indices $\alpha_l = 0.9$ and $\alpha_h = 1.93$ (see Table 1). Only $1/(1 + \tau_{\gamma\gamma})$ attenuation is depicted, and a variability size of $R = 3 \times 10^7 \Gamma^2 \text{ cm}$ was assumed. The peak flux evolution between the curves is by successive factors of $\sqrt{10}$ from top to bottom. The dotted curve illustrates a hard-to-soft evolution situation and is virtually coincident with the corresponding fixed $E_B = 0.4 \text{ MeV}$ case above the break, and below 500 GeV . The filled circle denotes the highest energy EGRET photon at $\sim 120 \text{ MeV}$ (see Table 1). The attenuation turnover energy E_t evolves, tracing out an $E_t^{-0.92}$ locus, as discussed in the text. As in Fig. 2, the MAGIC flux limit upper bounds for GRB 050713a (Albert et al. 2006a) are denoted by the heavy-weight histogram.

Finally, for this example, observe that since ε_B is not influential in determining the turnover energy, it was held constant for illustrative purposes. In Fig. 3, the dotted curve depicts a case where strong hard-to-soft evolution would arise subsequent to the peak flux snapshot. Well above ε_B , and below the recovery domain at $E \gtrsim 1 \text{ TeV}$, this curve is not distinguishable from the corresponding solid curve for the fixed ε_B case, since the target energies for photons near the turnover are above the break energy. In the $E \gtrsim 1 \text{ TeV}$ portion of the spectrum, the extra supply of target photons below 0.4 MeV relative to the $\varepsilon_B = 0.4 \text{ MeV}$ solid line case with the same $f(1 \text{ MeV})$ clearly enhances the pair opacity and lowers the spectrum accordingly. Fig. 3 encapsulates high energy spectral attenuation characteristics appropriate for constant Γ scenarios that admit evolution of

the break energy ε_B with time, and therefore possesses broader applicability. The import of this broad scope will soon become apparent, when scenarios incorporating Γ evolution with time are addressed just below. Observe also that while not illustrated in this example, evolution of α_h with time can be easily accommodated to provide useful diagnostics on Γ .

The simplest (but by no means uniquely preferred) case corresponding to appreciable reductions of Γ on a timescale of the burst duration is defined by the hydrodynamic sweep-up by a blast wave of exterior material from the interstellar medium or a progenitor wind. This is essentially the scenario explored by Rees and Mészáros (1992), and encapsulated nicely in the paper by Dermer, Chiang & Böttcher (1999). It is this latter analysis that is employed here, specifically the self-similar solution for blast wave deceleration in a uniform or spatially-structured circumburst environment. Assuming, for simplicity, that the density of material the blast wave impacts is uniform, then the sweep-up is precisely a relativistic extension of the classic Sedov-Taylor phase solution for supernova remnant expansion. This hydrodynamic problem for an expansion with an ultra-relativistic equation of state was treated by Blandford & McKee (1976). In the limit that the magnetic field plays a passive role, the conservation of energy and momentum in an adiabatically-expanding, non-radiative scenario yields a radial form for the deceleration of

$$\Gamma(r) \propto r^{-3/2} \propto t^{-3/8}, \quad t_{\text{dyn}} \ll t \ll t_{\text{rad}} \quad (43)$$

after the coasting phase has passed on a timescale of t_{dyn} . If the expansion is radiative, i.e. loses energy via radiation on times t_{rad} shorter than dynamical timescales t_{dyn} , then the evolution is described by a momentum-conserving “snowplow” form (e.g. Blandford & McKee 1976; Dermer, Chiang & Böttcher 1999)

$$\Gamma(r) \propto r^{-3} \propto t^{-3/7}, \quad t_{\text{rad}} \ll t_{\text{dyn}} \ll t. \quad (44)$$

The dynamical sweep-up scale ct_{dyn} is directly expressible in terms of the “explosion” energy \mathcal{E}_0 , the solid angle Ω_0 of collimated expansion, coasting phase (initial) Lorentz factor Γ_0 , and mass density ρ of the circumburst medium as

$$ct_{\text{dyn}} = \frac{1}{\Gamma_0^2} \left\{ \frac{3\mathcal{E}_0}{\Omega_0 \Gamma_0^2 \rho c^2} \right\}^{1/3}. \quad (45)$$

Here the presence of the Γ_0^2 factor out the front accounts for relativistic time dilation between the blast and observer’s frames (similar factors mediate the r - t coupling in Eqs. [43] and [44]), and the other Γ_0^2 factor couples to the energy conservation during sweep-up; these factors provide the only relativistic modification from the classic Sedov-Taylor phase timescale. Other radial/temporal dependences for Γ can be envisaged (e.g. Mészáros, Rees & Wijers 1998), for example that incurred by a power-law radial dependence for the circumburst density profile.

The forms in Eqs. (43) and (44) suffice for the purposes of this exposition, yielding time-dependence templates for scoping out pair creation attenuation signatures. Collimation of the outflow causally impacts the kinematic phase space only very late in the GRB afterglow. The other ingredients needed are the Lorentz factor dependences for the spectral break energy ε_B and the flux at this or some fixed higher energy. These quantities are model-dependent. Adhering to the prevailing paradigm that the GRB emission mechanism is synchrotron radiation, Dermer, Chiang & Böttcher (1999) argued in their external shock model that the break energy, if it corresponds to synchrotron photons from

electrons of the minimum Lorentz factor γ_{\min} in a non-thermal distribution, would behave according to

$$\varepsilon_B \propto [\Gamma(r)]^4 . \quad (46)$$

The origin of this form assumes that $\gamma_{\min} \propto \Gamma$ arises during energy transfer in the sweep-up phase, that the ambient magnetic field is boosted by Γ in the comoving frame, and also incorporates one power of Γ for the energy blueshift to the observer's frame. All these are reasonable contentions. Yet, it is clear that a sizeable fraction of bursts cannot generate low energy spectra consistent with the synchrotron mechanism using a cutoff distribution; this is the so-called ‘‘line of death’’ issue raised by Preece et al. (1998, 2000), discussed also in Baring & Braby (2004). Hence, the possibility of $\varepsilon_B(\Gamma)$ dependences other than in Eq. (46) can also be entertained.

The flux evolution with time or Lorentz factor is encapsulated in the third part of Eq. (20) of Dermer, Chiang & Böttcher (1999). Physically, this form assumes that there is prompt dissipation of a sizeable fraction the available energy, namely the energy of matter swept up in the deceleration phase. For environments where the circumburst medium is uniform, this form yields a temporal dependence for $\varepsilon \gg \varepsilon_B$ of

$$n(\varepsilon) \propto \varepsilon^{-\alpha_h} t^{-3\varphi/(8-\eta_r)} \propto \varepsilon^{-\alpha_h} \Gamma^\varphi \quad (47)$$

where

$$\varphi = 4\alpha_h - \frac{16}{3} + \frac{2}{3}\eta_r \quad (48)$$

is the index defining the bulk Lorentz factor dependence for the source flux, and

$$\eta_r = \begin{cases} 0 & , \text{adiabatic,} \\ 1 & , \text{radiative} \end{cases} \quad (49)$$

is the parameter that demarcates radiative and adiabatic expansion cases. Observe that with this definition, $\Gamma \propto t^{-3/(8-\eta_r)}$ describes the cases in Eqs. (43) and (44), so that the identity $g = 3/(2 - \eta_r)$ provides a connection to the parameter g that Dermer, Chiang & Böttcher (1999) use throughout their investigation, with $\Gamma \propto r^{-g}$. Observe also that inserting Eq. (46) into Eq. (47) yields

$$\varepsilon_B^2 n(\varepsilon_B) \propto t^{-1-3\eta_r/(8-\eta_r)} \propto \Gamma^{2(4+\eta_r)/3} , \quad (50)$$

commensurate with the evolution of the *peak flux* that is given in Eq. (16) of Dermer, Chiang & Böttcher (1999). Adiabatic expansions generate $\varepsilon_B^2 n(\varepsilon_B) \propto t^{-1} \propto \Gamma^{8/3}$, a form dictated by energy/momentum conservation in sweep-up, which because of scale-invariance is deducible directly from Eq. (45); radiative expansions produce $\varepsilon_B^2 n(\varepsilon_B) \propto t^{-10/7} \propto \Gamma^{10/3}$. The flux evolution prescribed by Eq. (47) can be easily modified to accommodate expansions into non-uniform circumburst media, yet suffices for the illustrative purposes of this paper.

It should be noted that while the temporal evolution employed in Dermer, Chiang & Böttcher (1999) envisages an external shock model for the prompt emission, and can directly be applied to afterglow considerations, it is also germane for internal shock models if the gamma-ray activity arises during a deceleration epoch. Then, the colliding shocks would possess different Lorentz factors, which would on average slow down with the expansion. The relevant Γ for the purposes of this analysis would then be some average of those of the colliding shells, and would be controlled by the hydrodynamics discussed just above.

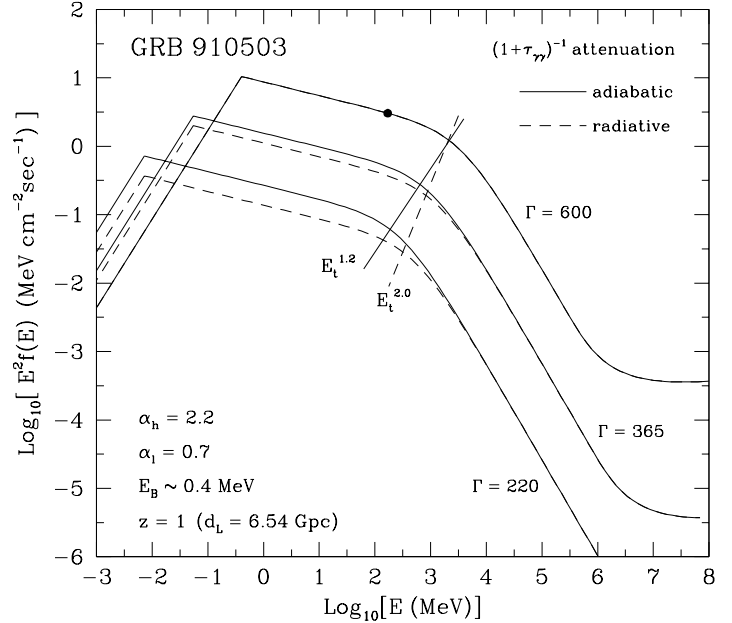


FIG. 4.— An evolving sequence depicting γ - γ attenuation, internal to the source, for GRB 910503, again assuming a redshift $z = 1$ typical of long duration bursts. The source spectrum (in $\varepsilon^2 f(\varepsilon)$ format) was a power-law broken initially at $E_B = 0.4$ MeV (uppermost solid and dashed curves that are coincident), with spectral indices $\alpha_l = 0.7$ and $\alpha_h = 2.2$ (see Table 1) that are maintained throughout. For this initial case, the bulk Lorentz factor was $\Gamma = 600$. The highest energy EGRET photon at ~ 170 MeV (Schneid et al. 1992) is denoted by the filled circle. Again only $1/(1 + \tau_{\gamma\gamma})$ attenuation is depicted, and a variability size of $R = 3 \times 10^7 \Gamma^2$ cm was assumed. The peak flux and hard-to-soft evolution between the curves is indicated via declining Lorentz factors, i.e., cases $\Gamma = 365$ and $\Gamma = 220$ as labelled. The hard-to-soft evolution of the break energy ε_B is prescribed via Eq. (46), while the flux evolution is given in Eq. (47), and is discussed in the text. Solid curves correspond to adiabatic blast wave deceleration, for which the attenuation turnover energy approximately traces out [see Eq. (52)] the depicted $E_t^{1.2}$ locus, while dashed curves illustrate a strongly radiative case, for which the locus of $\tau_{\gamma\gamma} = 1$ turnover points is the illustrated $E_t^{2.0}$ line.

Representative spectra for evolving Γ scenarios are exhibited in Fig. 4 for the case of GRB 910503. This elaborates upon the evolutionary sequence addressed in Baring (2001) for GRB 930131. Here α_l and α_h are held constant, so as to simply demonstrate the key characteristics, though for some bursts (e.g. see Gonzalez et al. 2004) there are significant variations of α_h with time. The flux and break energy evolve according to Eqs. (46) and (47) respectively, and in this example $\varepsilon_c = 0$. Notably, the turnover energies are now declining functions of time, contrasting the constant Γ example in Fig. 3, for which the turnover locus is $E_t^{3-2\alpha_h}$. This behavior is obviously caused by the increased opacity due to the decline of Γ , which more than offsets the tendency of a reduced flux at typical super-MeV target photon energies to reduce the pair opacity. Such a signature renders it easy to discriminate GRB environs where bulk deceleration is prevalent during the prompt phase, from the case of constant Γ , where internal shock dissipation is completely decoupled from external shock evolutionary dynamics. This is a powerful observational diagnostic that is only modified in detail, but not in character, by model nuances such as spatial non-uniformity in the circumburst medium.

A comparison of the solid and dashed curves in Fig. 4 indicates that it will be harder to discern between adiabatic and radiative evolutionary scenarios, though it may be marginally

possible. The tracks of the spectrum around the break energy do not distinguish substantially between the $\eta_r = 0$ and $\eta_r = 1$ cases in that the separation of fluxes for given break energy is only modest, and break smoothing could render such trends indistinguishable. The turnover feature adds extra information that is helpful, provided that the hard gamma-ray continuum is detected with sufficient significance over around at least 2 decades of flux evolution at above 1 GeV. The Figure marks two loci that the turnovers trace in time for the respective adiabatic and radiative cases. As for the constant Γ case, these loci define the correlation between evolution of the BATSE-band flux and the turnover energy E_t , which can again be found using the last term in Eq. (29) as the dominant contribution to $\tau_{\gamma\gamma}$. One finds that $\tau_{\gamma\gamma} \propto f(1 \text{ MeV}) E_t^{\alpha_h - 1} / \Gamma^{\lambda + 2\alpha_h}$, where $\lambda = 1, 2$ is the index defining the Lorentz contraction relating the perceived source size to the variability timescale. From this, and Eq. (47), it follows that the turnover energy satisfies

$$E_t \propto \Gamma^{(\lambda + 2\alpha_h - \varphi)/(\alpha_h - 1)}, \quad (51)$$

expressing the $\tau_{\gamma\gamma} \sim 1$ criterion, with φ as defined in Eq. (48). Inverting this result and combining it with Eq. (47), the time-dependent spectral form valid far above the break energy ε_B , results in

$$E_t^2 f(E_t) \propto E_t^\varrho, \quad \varrho = 2 - \alpha_h + \frac{\varphi(\alpha_h - 1)}{\lambda + 2\alpha_h - \varphi} \quad (52)$$

as the mathematical form for the locus of turnover points in νF_ν space. For GRB 910503 with $\alpha_h = 2.2$, and assuming $\lambda = 2$, this approximately generates $E_t^{1.2}$ for the adiabatic case ($\eta_r = 0$) and $E_t^{2.0}$ for radiative regimes ($\eta_r = 1$), which are represented by the lightweight solid and dashed lines in Fig. 4. These are clearly distinct, and offer the attractive possibility of discriminating between adiabatic and radiative evolutionary scenarios for a given burst, particularly if explored in conjunction with the ε_B evolution.

Since ϱ is a rapidly increasing function of α_h , flat-spectrum bursts with high super-100 MeV fluxes offer the most promising discrimination: $\alpha_h = 2$ yields $\varrho = 4/5$ for adiabatic ($\eta_r = 0$) regimes, and $\varrho = 5/4$ for radiative ones ($\eta_r = 1$). However, note that when adopting a variability size of $R = 3 \times 10^7 \Gamma \text{ cm}$ (i.e., $\lambda = 1$), the loci in Fig. 4 change significantly, to approximately $E_t^{1.95}$ and $E_t^{3.7}$ for adiabatic and radiative cases, respectively. Hence, in practice it may prove difficult to cleanly distinguish between the effects of non-adiabaticity in the expansion and the nature of structure in the emission region using the turnover energy as a diagnostic. Using the sub-MeV band temporal traces of the break energy in conjunction should help separate these competing influences.

4. THE POTENTIAL FOR OBSERVATIONAL DIAGNOSTICS

As a benchmark for the GRB phase space that is germane to internal $\gamma\gamma$ opacity diagnostics by GLAST and perhaps atmospheric Čerenkov telescopes, and future experiments down the line, one can map the contours the turnover energies trace for burst parameters typical of the bright sources EGRET that detected. For given Γ and α_h , the maximum photon energy $E_{\text{MAX}} = E_t$ (in MeV) attainable in the EGRET-band power-law, before pair attenuation turnovers appear, is simply determined by noting that the spectral structure at and below the BATSE-band break is immaterial to its evaluation. Therefore, one can set $\varepsilon_B \rightarrow 0$ in the analysis, and then impose a $\tau_{\gamma\gamma} \sim 1$

criterion to establish, using Eqs. (6) and (17), that

$$E_{\text{MAX}} = \frac{0.511 \Gamma^{2\alpha_h/(\alpha_h - 1)}}{\left\{ n_\gamma \sigma_T R \mathcal{A}(\alpha_h) \mathcal{H}(\alpha_h, 1) \right\}^{1/(\alpha_h - 1)}} \text{ MeV} \quad (53)$$

This energy is plotted as a function of α_h for different Γ and fluxes $f(1 \text{ MeV})$ in Fig. 5, specifically for source luminosity distances of 6.54 Gpc (i.e. $z = 1$). Such curves were determined assuming a variability size of $R = 3 \times 10^7 \Gamma^2 \text{ cm}$, and are applicable for both $1/(1 + \tau_{\gamma\gamma})$ attenuation and exponential attenuation. This depiction represents an update of Figure 6 of Baring and Harding (1997b) that reflects the moderate redshifts now associated with GRBs in the Swift/HETE era; Jakobsson et al. (2006) report a mean redshift of $z \sim 2.8$ in their compilation of 16 Swift bursts with measured redshifts.

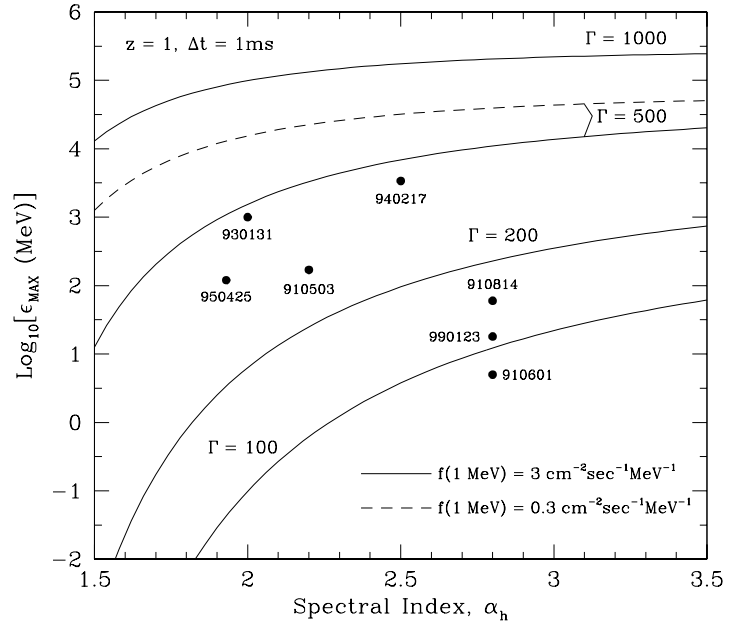


FIG. 5.— The phase space diagram for the observational parameters E_{MAX} and α_h , consisting of contours of constant Γ , as labelled. The contours correspond to solutions in Eq. (53) of $\tau_{\gamma\gamma} = 1$. Here $z = 1$, and a variability size of $R = 3 \times 10^7 \Gamma^2 \text{ cm}$ was adopted. The solid and dashed ($\Gamma = 500$ case only) contours correspond to the indicated choices of the flux $f(1 \text{ MeV})$ at 1 MeV. The observed EGRET values of E_{MAX} and α_h for the seven bursts in Table 1 are plotted as points; these bursts all have values of $f(1 \text{ MeV})$ somewhat different from the chosen contour values.

The E_{MAX} curves are monotonically increasing functions of α_h and Γ , and are decreasing functions of $f(1 \text{ MeV})$, as indicated by comparison of the solid and dashed $\Gamma = 500$ examples. Since the optical depth is fixed at unity at the turnover energy, and the flux is pinned at 1 MeV, thereby providing a “pivot point” in the spectrum, increasing α_h then lowers the number of interacting photons above pair threshold (generally above 1 MeV in the observer’s frame) so that E_{MAX} correspondingly increases to compensate. The depiction of $(\alpha_h, E_{\text{MAX}})$ positions for the EGRET bursts listed in Table 1 clearly indicates that $\Gamma \gtrsim 100$ in their emission regions if they are all at or near a redshift of $z = 1$. Observations of further extension of their power-laws by GLAST could push these Lorentz factor bounds considerably higher: much of the phase space below $E_{\text{MAX}} \sim 10^4 \text{ MeV}$ and $\alpha_h \lesssim 2.5$ is readily accessible to GLAST, underlining its potential as a tool for probing GRB bulk motion characteristics. As the hard gamma-ray spectral index increases to $\alpha_h \gtrsim 2.8$,

the total photon counts collected by the LAT instrument will correspondingly be reduced, lowering the maximum energies to which it can probe to below 1 GeV.

The results of Section 3.2 highlight one and possibly two groundbreaking probes of the burst environment by hard gamma-ray experiments that explore the GLAST window. First, the comparison of Figs. 3 and 4 offers strikingly different evolution of the turnover energy E_t with time (i.e., declining MeV-band flux) for constant Γ and evolving Γ scenarios. A sensitive hard gamma-ray detector would easily be able to discern between these two signatures, using data binned into several time windows, and cast light on the Γ evolution for a number of bright, energetic bursts. Moreover, these internal absorption signatures can be easily distinguished from external absorption characteristics due to background fields, which generate turnover energies independent of time or MeV-band flux.

This tracking of Γ evolution is a global possibility that is not confused by specific model nuances such as circumburst non-uniformity and departures from temporal monotonicity for the flux. Should a burst exhibit $\Gamma = \text{const.}$ behavior, it can be concluded that the expansion timescale is shorter than the dynamical one, so that the burst duration T_{90} in conjunction with Eq. (45) can be used to provide an approximate lower bound to the explosion energy \mathcal{E}_0/Ω_0 per unit solid angle of the expansion, modulo the density of the environment surrounding the burst:

$$\frac{\mathcal{E}_0}{\Omega_0} \gtrsim U_0 \equiv \frac{1}{3} \Gamma_0^8 \rho c^5 T_{90}^3, \quad \Gamma = \Gamma_0 = \text{const.} \quad (54)$$

On the other hand, should Γ changes be observed, whether increasing or declining with time, one could argue that the dynamical timescale is smaller than the expansion age and that $\Gamma < \Gamma_0$. Accordingly, an upper bound $\mathcal{E}_0/\Omega_0 \lesssim U_0$ on the collimated explosion energy would be obtained, and this could be tightened to an approximate estimate $\mathcal{E}_0/\Omega_0 \sim \Gamma^8 \rho c^5 T_{90}^3$, with considerable uncertainty due to the spread in Γ estimates derived from the pair attenuation turnovers. This calibration of \mathcal{E}_0/Ω_0 is analogous to inferences made in non-relativistic supernova remnant expansions either in the coasting or Sedov phase. Furthermore, if a radiative regime is deduced to be operating, then hard gamma-ray observations can also constrain pertinent environmental parameters for a chosen radiation mechanism, via bounds on the cooling timescale. Notwithstanding, it is noted that marked variations of α_h with time can degrade this diagnostic possibility. Such a property is evinced in spectroscopy analyses of some bursts (see, for example, the joint BATSE/EGRET TASC study of Gonzalez et al. 2004), though the average characteristics of time-resolved α_h determinations by BATSE are similar to the time-integrated α_h values (e.g. Kaneko et al. 2006). GLAST will solidify the understanding of temporal variations, or otherwise, in α_h for many bursts.

An interesting, though somewhat less promising diagnostic is the discrimination between adiabatic and radiative/non-adiabatic evolutionary scenarios. While the evolutionary loci of E_t for these cases are distinct in Fig. 4, they are only modestly so, and can easily be blurred by breadth of the turnover, the influence of non-uniformities in the burst environs, or complicated variability in the spectral shape with time. Furthermore, significant changes in the value of the index ϱ in Eq. (52) are incurred in going from longitudinal ($\lambda = 2$) to transverse variability ($\lambda = 1$) situations. Hence it becomes harder to disentangle a variety of effects given an observed, evolving, GeV-band spectrum. Degeneracies can be partially removed by exploring

correlations with the MeV-band peak evolution, in both flux and break energy. For example, Eqs. (46) and (50) combine to give a locus of breaks whose slope depends only on η_r , and is independent of α_h . How effective such a correlated diagnostic will be will depend on the sharpness of the respective breaks.

GLAST's Large Area Telescope (LAT) offers potential for exploring these signatures, being considerably more sensitive than EGRET; its principal capability will be to provide lower bounds to Γ via its refinement of E_{MAX} , and perhaps also the first observations of turnovers in the brightest subset of the burst population (e.g. see Omodei et al. 2006, for simulated spectra with detectable turnovers). Band, et al. (2004) and Cohen-Tanugi, et al. (2004) provide brief outlines of the anticipated performance of GLAST for burst detections. Being ephemeral in nature, GRBs are vastly different from steady sources, for which the LAT Performance Web Page http://www-glast.slac.stanford.edu/software/IS/glast_lat_performance.htm offers putative integral sensitivities for the 5σ detection of a high latitude source above a given energy, resulting from a one-year, all-sky survey. With the average 2 steradian field of view for the LAT, this corresponds to around $t_{1\text{yr}} = 5 \times 10^6$ seconds observing a given source, far above the typical duration of bursts. For steady sources, background is an issue (especially in the galactic plane: see Hunter et al. 1997, for the presentation of EGRET background determinations), but its influence on the observability for bursts virtually disappears since they are of such short duration. Gamma-ray burst detectability by the LAT correlates to the total number of photons counted above its threshold energy of 30 MeV. Potential instrumental deadtime due to data readout after triggers is small, about 5%. LAT Team simulations of detector sensitivities (Omodei, et. al. 2006) indicate that only a handful of bursts seen by GLAST each year will provide several hundred photon counts in the LAT above the threshold of 30 MeV, and perhaps one a year with of the order of a 1000 or so (and around one a year with 100 photons above 1 GeV). Such cases could, in principal, yield of the order of 30–100 photons above 300 MeV if the burst possesses a flat E^{-2} spectrum. Observing turnovers around 100 MeV–1 GeV would then be viable with such a database, and moreover, it may prove possible to track spectral evolution at around 100 MeV–1 GeV by binning data in two or three time intervals, with corresponding flux reductions by a factor of 2–5 in the MeV band (or at higher energies).

Such is the optimal situation. Nature, of course, may not provide turnovers at such low energies, so GLAST's potential for casting light on the above bulk Lorentz factor diagnostics will only truly be known after launch. Yet, bright EGRET bursts typically have flat spectra, on average around E^{-2} (see Dingus, 1995, for a compilation encompassing most of the bursts considered in this paper), which may or may not be the result of flux selection effects at higher energies. These are ideal candidates for exploring spectral turnovers in the super-GeV band, which were simulated by the LAT Collaboration in Omodei et al. (2006). At best, only an elite handful of bursts over the GLAST lifetime might be amenable to observing both turnovers in the sub-GeV band, and partially tracking their evolution with time. This number will increase if the bulk Lorentz factors are actually slightly lower than those used in the illustrations here. Accordingly, GLAST might be capable of performing some of the GRB source diagnostics discussed in the text. In addition, the diagnostics identified in this paper look to the future, providing science motivations for next generation hard gamma-ray detectors, both of the space-based variety and also ground-based

Čerenkov arrays. Since the atmospheric Čerenkov technique is intrinsically the more sensitive, due to its much greater collection area, the current push to lower their thresholds deep into the GLAST band via increased telescope mirror size may influence the direction gamma-ray burst observational programs targeting energies above 1 GeV will take. This advantage is offset by their generally small fields of view (except for water tank Čerenkov systems such as MILAGRO), so that large fields of view like those afforded by the LAT and the Gamma-Ray Burst Monitor (GBM) on GLAST are desirable.

5. CONCLUSION

This paper outlines the interesting potential the GLAST mission and future hard gamma-ray detectors can offer for probing the relativistic nature of outflow in gamma-ray burst prompt emission regions. The diagnostics highlighted here use a single, straightforward piece of physics, namely that of electron-positron pair creation, and are only dependent on model assumptions to second order. Spectral attenuation by this process, while not evident in EGRET data for a handful of bright, hard bursts, should emerge from the GLAST database, unless the bulk Lorentz factors in the burst emission zones are higher than presently argued, i.e. greater than around $\Gamma \sim 10^3$. Then, attenuation by interaction of source photons with those of the intervening cosmic background field will produce attenuation turnovers at above 30–50 GeV, whose energies are independent of the GRB flux at a given time. In such cases, bursts can be used to explore the evolution of the background field with redshift by detectors with sufficient sensitivity in this band.

For the equally interesting possibility of lower Γ , pair creation turnovers spawned by photons internal to the burst, will become prominent in the GLAST energy window. In such cases, the representative calculations in Section 3 clearly illustrate how the LAT instrument on GLAST might potentially discriminate between evolutionary scenarios with constant Γ , and those where Γ declines with time, should Nature be agreeable and offer bright, hard bursts with turnovers below 300 MeV–1

GeV. A more sensitive, next-generation hard gamma-ray experiment might additionally be capable of distinguishing between adiabatic and radiative evolutionary scenarios: due to their different $\Gamma(t)$ dependence, their turnover energy/flux loci trace somewhat different tracks over time. However, this probe will be more reliable for flat spectrum bursts and require relatively sharp turnovers, or correlated information from the MeV-band break evolution. While the GBM on GLAST, in conjunction with the LAT, while accumulate a host of data on the MeV-band break evolution, next-generation telescopes most likely will be needed to differentiate the adiabatic and radiative turnover tracks. Should distinction between these two keystone classes of blast wave deceleration be possible, the pair creation probes offer constraints on the explosion energy generated by the central engine. Note that while the results presented focus on simple broken power-law source spectra, they are readily extended to apply to multiple components. They encompass a variety of possibilities, and provide a template for burst pair production attenuation studies in the soon-to-be realized GLAST era, and for future initiatives down the line.

I thank Alice Harding for many interactions over the years on pair attenuation in bursts, for carefully reading the manuscript and providing incisive suggestions for the clarification of certain points. I thank Seth Digel for extensive discussions on GLAST/LAT sensitivity expectations, Jay Norris and David Band for insights into GLAST/LAT capabilities for gamma-ray burst detections, and Brenda Dingsus for reading through the paper and providing updates on atmospheric Čerenkov telescope observations of GRBs. I also thank the referee, Peter Mészáros for recommendations helpful in the polishing of the manuscript. This research was supported in part by the National Science Foundation under Grant Nos. AST00-98705 and PHY99-07949, and I acknowledge the hospitality of the Kavli Institute for Theoretical Physics, University of California, Santa Barbara, where part of the work for this paper was performed.

APPENDIX

INTEGRATION OF THE ANGULAR CONTRIBUTIONS TO $\tau_{\gamma\gamma}(\varepsilon)$ FOR STRONG BEAMING

Here the analytic reduction of the triple integration in Eq. (15) is outlined, together with relevant properties of the emergent hypergeometric function. It is expedient to scale the integration variables via $x_\omega = wx_\varepsilon$ and $\kappa = x_\varepsilon\rho$, so that x_ε , w and ρ constitute the new set of integration variables. Then, one performs the w integration first, which is easily tractable, and generates a simple evaluation in terms of inverse trigonometric functions using identity 2.261 of Gradshteyn & Ryzhik (1980). The x_ε integration is then trivial, absorbing the constraints imposed by the step function $\Theta[\kappa\eta\theta_m/(2\chi)]$. The result can then be expressed (for $0 \leq \Psi \leq 1$) as

$$\mathcal{F}_\alpha \approx \theta_m^{2\alpha} \mathcal{G}_\alpha(\Psi) \quad , \quad \mathcal{G}_\alpha(\Psi) = \frac{16}{\pi(\alpha+2)} \left\{ \int_0^\Psi dy y^{1+2\alpha} \arccos y + \Psi^{2(\alpha+2)} \int_\Psi^1 \frac{dy}{y^3} \arccos y \right\} \quad , \quad (\text{A1})$$

with now the one parameter

$$\Psi = \frac{\chi}{\eta\theta_m} \quad (\text{A2})$$

defining the general character of \mathcal{F}_α . From this form, the substitution $y = \sin\beta$ and the invocation of identities 3.621 and 8.335.1 of Gradshteyn & Ryzhik (1980) lead to the result in Eq. (16) when $\Psi = 1$. On the other hand, the $\Psi \ll 1$ limit is readily discerned, thereby reproducing Eq. (18). These two cases correspond to the results

$$\mathcal{G}_\alpha(1) = \mathcal{A}(\alpha) \quad , \quad \text{and} \quad \mathcal{G}_\alpha(\Psi) \sim \frac{4}{\alpha+1} \Psi^{2(1+\alpha)} \quad , \quad \Psi \ll 1 \quad . \quad (\text{A3})$$

For $\Psi > 1$, corresponding to cases where the angular integrations are completely separated from the threshold constraint, $\mathcal{G}_\alpha(\Psi) = \mathcal{G}_\alpha(1) = \mathcal{A}(\alpha)$. For general $0 \leq \Psi < 1$, the integrals for $\mathcal{G}_\alpha(\Psi)$ can be manipulated by the appropriate integration by parts, and then the second integral term in Eq. (A1) is routinely handled. The first integral is somewhat more complicated, and can be developed by using the change of variables $y = \Psi \cos x$ together with the aid of the result 3.671 of Gradshteyn & Ryzhik (1980). This renders the first integral expressible in terms of the ordinary hypergeometric function $F \equiv {}_2F_1$, so that

$$\mathcal{G}_\alpha(\Psi) = \frac{8}{\pi} \Psi^{2(1+\alpha)} \left\{ \frac{\arccos \Psi}{\alpha+1} - \frac{\Psi \sqrt{1-\Psi^2}}{\alpha+2} + \frac{\Psi F(1/2, \alpha+3/2; \alpha+5/2; \Psi^2)}{(\alpha+1)(2\alpha+3)(\alpha+2)} \right\}, \quad 0 \leq \Psi \leq 1. \quad (\text{A4})$$

This hypergeometric function reduces to combinations of inverse trigonometric and algebraic functions when α assumes integer values, and just algebraic functions when α takes on half integral values. For this range of Ψ , the hypergeometric function can be numerically evaluated using the series expansion 9.100 of Gradshteyn & Ryzhik (1980), yielding

$$F\left[\frac{1}{2}, \alpha + \frac{3}{2}; \alpha + \frac{5}{2}; z\right] = \sum_{n=0}^{\infty} a_n z^n, \quad a_n = \frac{2\alpha+3}{2\alpha+2n+3} \prod_{k=1}^n \left(1 - \frac{1}{2k}\right). \quad (\text{A5})$$

For $0 \leq z < 1$, this series converges rapidly, faster than a geometric series. In the boundary case of $z = 1$, convergence is only moderately rapid. The asymptotic behavior of the product in Eq. (A5) as $n \rightarrow \infty$ can be established by taking its logarithm and then using the series identity 44.9.1 of Hansen (1975):

$$\sum_{k=1}^{\infty} \left[\frac{x}{k} - \log_e \left(1 + \frac{x}{k}\right) \right] = \gamma_E x + \log_e \Gamma(x+1), \quad (\text{A6})$$

where $\Gamma(z)$ is the Gamma function, and $\gamma_E = -\psi(1) \approx 0.57721$ is the Euler-Mascheroni constant, with $\psi(z) = d/dz \{\log_e \Gamma(z)\}$. By truncating the resultant infinite series and then invoking results 8.365.3 and 8.365.5 of Gradshteyn & Ryzhik (1980), the $n \rightarrow \infty$ limit can eventually be taken, thereby deriving the result

$$\lim_{n \rightarrow \infty} \sqrt{n} \prod_{k=1}^n \left(1 - \frac{1}{2k}\right) = \frac{1}{\sqrt{\pi}}. \quad (\text{A7})$$

Hence, the series expansion in Eq. (A5) converges as $n^{-3/2}$ for large n . Such a rate of convergence is not compelling, so that for values $z \approx 1$ it is more expedient to perform the transformation indicated in 9.131.2 of Gradshteyn & Ryzhik (1980), and then use the resultant identity

$$F\left[\frac{1}{2}, \alpha + \frac{3}{2}; \alpha + \frac{5}{2}; z\right] = \sqrt{\pi} \frac{\Gamma(\alpha+5/2)}{\Gamma(\alpha+2)} F\left[\frac{1}{2}, \alpha + \frac{3}{2}; \frac{1}{2}; 1-z\right] - (2\alpha+3) \sqrt{1-z} F\left[1, \alpha+2; \frac{3}{2}; 1-z\right] \quad (\text{A8})$$

to evaluate the left hand side for domains of $(1-z) \ll 1$. The rate of convergence of the two hypergeometric functions on the right hand side of Eq. (A8) is then at least as rapid as a geometric series. This transformation also expeditiously establishes the correspondence $\mathcal{G}_\alpha(\Psi) \rightarrow \mathcal{A}(\alpha)$ as $\Psi \rightarrow 1^-$, using the doubling formula (8.335.1 of Gradshteyn & Ryzhik 1980) for the Gamma function. For numerical purposes, it is obviously convenient to use Eq. (A5) for $0 \leq z \leq 1/2$ cases, and the power series expansion about $z = 1$ of the right hand side of Eq. (A8) when $1/2 < z \leq 1$.

To conclude, two integrals that are required for the determination of the asymptotic approximation for $\mathcal{T}(\theta_m, \eta)$ when $\eta\theta_m \gg 1$ are evaluated. Using the integral form for $\mathcal{G}_\alpha(\Psi)$ in Eq. (A1), it can be quickly demonstrated that

$$\int_0^1 \frac{d\Psi}{\Psi^{1+2\alpha}} \mathcal{G}_\alpha(\Psi) = \frac{1-\mathcal{A}(\alpha)}{2\alpha}, \quad \int_0^1 d\Psi \frac{\log_e \Psi}{\Psi^{1+2\alpha}} \mathcal{G}_\alpha(\Psi) = \frac{1-\mathcal{A}(\alpha)}{4\alpha^2} - \frac{4 \log_e 2 + 1}{8\alpha} \quad (\text{A9})$$

by appropriate integration by parts to generate the derivative $d\mathcal{G}_\alpha/d\Psi$ in each case.

REFERENCES

- Aharonian, F., et al. 2006, *Nature*, 440, 1018.
 Albert, J., et al. 2006a, *ApJ*, 641, L9.
 Albert, J., et al. 2006b, *ApJ*, 642, L119.
 Atkins, R., et al. 2000, *ApJ*, 533, L119.
 Atkins, R., et al. 2003, *ApJ*, 583, 824.
 Atkins, R., et al. 2005, *ApJ*, 630, 996.
 Band, D. L., et al. 1993, *ApJ*, 413, 281.
 Band, D. L., et al. 2004, in *Gamma-Ray Bursts: 30 years of Discovery*, eds. Fenimore, E. E. & Galassi, M. (AIP Conf. Proc. 727, New York) p. 692.
 Baring, M. G. 1993, *ApJ*, 418, 391.
 Baring, M. G. 1994, *ApJS*, 90, 899.
 Baring, M. G. 2001, in *Gamma-Ray Astrophysics*, eds. S. Ritz, N. Gehrels & C. Schrader (AIP Conf. Proc. 587, New York), p. 153.
 Baring, M. G. & Braby, M. L. 2004, *ApJ*, 613, 460.
 Baring, M. G. and Harding, A. K. 1996, in *Gamma-Ray Bursts*, eds. Kouveliotou, C., Briggs, M. S., and Fishman, G. J. (AIP Conf. Proc. 384, New York) p. 724.
 Baring, M. G. & Harding, A. K. 1997a, *ApJ*, 481, L85. (BH97a)
 Baring, M. G. & Harding, A. K. 1997b, *ApJ*, 491, 663.
 Bednarz, J. & Ostrowski, M. 1998, *Phys. Rev. Lett.*, 80, 3911.
 Berger, E., et al. 2006, *ApJ*, 642, 979.
 Blandford, R. D. & McKee, C. F., 1976, *Phys. Fluids*, 19, 1130.
 Briggs, M. S., et al. 1999, *ApJ*, 524, 82.

- Catelli, J. R., Dingus, B. L. & Schneid, E. J. 1996, in *Gamma-Ray Bursts*, eds. Kouveliotou, C., Briggs, M. F., and Fishman, G. J. (AIP Conf. Proc. 384, New York) p. 158.
- Cohen-Tanugi, J., et al. 2004, in *Third Rome Workshop on Gamma-Ray Bursts in the Afterglow Era*, eds. Feroci, M., Frontera, F., Masetti, N. & Piro, L. (ASP Conf. Ser. 312) p. 520.
- Connaughton, V., et al. 1997, ApJ, 479, 859.
- Crider, A. & Liang, E. P. 1999, A&AS, 138, 405.
- Cummings, J., et al. 2005, GCN 3910.
- Dermer, C. D., Chiang, J. & Böttcher, M. 1999, ApJ, 513, 656.
- Dermer, C. D., Chiang, J. & Mitman, K. E. 2000, ApJ, 537, 785.
- Dingus, B. L. 1995, Ap&SS, 231, 187.
- Epstein, R. I. 1973, ApJ, 183, 593.
- Epstein, R. I. 1985, ApJ, 297, 555.
- Fenimore, E. E., Epstein, R. I. & Ho, C.: 1992 in *Gamma-Ray Bursts*, eds. Paciesas, W. S. & Fishman, G. J., (AIP Conf. Proc. 265, New York) p. 158.
- Ford, L. A., et al. 1995, ApJ, 439, 307.
- González, M. M., Dingus, B. L., Kaneko, Y., Preece, R. D. & Briggs, M. S. 2004, in *Gamma-Ray Bursts: 30 Years of Discovery*, eds. Fenimore, E. E. & Galassi, M., (AIP Conf. Proc. 727, New York) p. 236.
- Gould, R. J. & Schreder, G. P. 1967, Phys. Rev., 155, 1404.
- Gradshteyn, I. S. & Ryzhik, I. M. 1980, *Table of Integrals, Series and Products*, (Academic Press, New York).
- Haislip, J., et al. 2006, Nature, 440, 181.
- Hanlon, L. O., et al. 1994, A&A, 285, 161.
- Hansen, E. R. 1975, *A Table of Series and Products*, (Prentice-Hall, Englewood Cliffs)
- Hjorth, J., et al. 1999, GCN Circular 219.
- Hunter, S. D., et al. 1997, ApJ, 481, 205.
- Hurley, K., et al. 1994, Nature, 372, 652.
- Jakobsson, P. et al. 2006, A&A, 447, 897.
- Jarvis, A., et al. 2005, Proc. 29th Int. Cosmic Ray Conf. (Pune), 4, 455.
- Kaneko, Y., et al. 2006, in *Gamma Ray Bursts in the Swift Era*, eds. Holt, S. S., Gehrels, N. & Nousek, J. (AIP Conf. Proc., New York), p. 133.
- Katz, J. I. 1994, ApJ, 432, L27.
- Kawai, N., et al. 2005, GCN 3937.
- Kirk, J. G., Guthman, A. W., Gallant, Y. A., Achterberg, A. 2000, ApJ, 542, 235.
- Kneiske, T. M., Mannheim, K. & Hartmann, D. 2002, A&A, 386, 1.
- Kouveliotou, C., et al. 1994, ApJ, 422, L59.
- Krolik, J. H. & Pier, E. A. 1991, ApJ, 373, 277.
- Kwok, P. W., et al. 1993, in *Compton Gamma-Ray Observatory*, eds. Friedlander, M., Gehrels, N., and Macomb, D. (AIP Conf. Proc. 280, New York) p. 855.
- Lithwick, Y. & Sari, R. 2001, ApJ, 555, 540.
- Longair, M. S. 1998, *Galaxy Formation*, (Springer-Verlag, Berlin)
- MacMinn, D. & Primack, J. 1996, Space Sci. Rev., 75, 413.
- Mannheim, K., Hartmann, D. & Funk, B. 1996, ApJ, 467, 532.
- Meegan, C., et al. 1996, ApJS, 106, 65.
- Mészáros, P. & Rees, M. J. 1994, MNRAS, 269, L41.
- Mészáros, P., Rees, M. J. & Wijers, R. A. M. J. 1998, ApJ, 499, 301.
- Mészáros, P., Rees, M. J. & Papathanassiou, H. 1994, ApJ, 432, 181.
- Omodei, N., et al. 2006, to appear in *Gamma Ray Bursts in the Swift Era*, eds. Holt, S. S., Gehrels, N. & Nousek, J. (AIP Conf. Proc., New York), p. 642.
- Perlmutter, S., et al. 1997, ApJ, 483, 565.
- Preece, R. D., et al. 1995, Ap&SS, 231, 149.
- Preece, R. D., et al. 1998, ApJ, 506, L23.
- Preece, R. D., et al. 2000, ApJS, 126, 19.
- Primack, J., Somerville, R. S., Bullock, J. S. & Devriendt, J. E. G. 2001, in *High Energy Gamma-Ray Astronomy*, eds. F. Aharonian & H. Völk, (AIP Conf. Proc. 558, New York), p. 463.
- Rees, M. J. & Mészáros, P. 1992, MNRAS, 258, 41P.
- Riess, A. G., et al. 1998, AJ, 116, 1009.
- Sari, R. & Esin, A. 2001, ApJ, 548, 787.
- Schaefer, B. E., et al. 1992, ApJ, 393, L51.
- Schmidt, W. K. H. 1978, Nature, 271, 525.
- Schneid, E. J. 1992, Astron. Astr. (Lett.), 255, L13.
- Sommer, M., et al. 1994, ApJ, 422, L63.
- Spergel, D. N., et al. 2003, ApJS, 148, 175.
- Stecker, F. W. 2001, in Proc. IAU Symposium 204, eds. M. Harwit & M. G. Hauser, p. 135.
- Stecker, F. W. & De Jager, O. C. 1996, Space Sci. Rev., 75, 401.
- Stecker, F. W., De Jager, O. C. & Salamon, M. H. 1996, ApJ, 390, L49.
- Stepney, S. & Guilbert, P. W. 1983, MNRAS, 204, 1269.
- Svensson, R. 1987, MNRAS, 227, 403.
- Woods, E. & Loeb, A. 1995, ApJ, 453, 583.